



저작자표시-비영리-변경금지 2.0 대한민국

이용자는 아래의 조건을 따르는 경우에 한하여 자유롭게

- 이 저작물을 복제, 배포, 전송, 전시, 공연 및 방송할 수 있습니다.

다음과 같은 조건을 따라야 합니다:



저작자표시. 귀하는 원저작자를 표시하여야 합니다.



비영리. 귀하는 이 저작물을 영리 목적으로 이용할 수 없습니다.



변경금지. 귀하는 이 저작물을 개작, 변형 또는 가공할 수 없습니다.

- 귀하는, 이 저작물의 재이용이나 배포의 경우, 이 저작물에 적용된 이용허락조건을 명확하게 나타내어야 합니다.
- 저작권자로부터 별도의 허가를 받으면 이러한 조건들은 적용되지 않습니다.

저작권법에 따른 이용자의 권리는 위의 내용에 의하여 영향을 받지 않습니다.

이것은 [이용허락규약\(Legal Code\)](#)을 이해하기 쉽게 요약한 것입니다.

[Disclaimer](#)

공학박사학위논문

음향 가진에 대한 다양한 H<sub>2</sub>/CH<sub>4</sub> 연료 조성의  
Burke-Schumann 화염의 응답 특성

The Response of the Burke-Schumann Flame of H<sub>2</sub>/CH<sub>4</sub>  
fuel to Acoustic Excitations

2018 년 8 월

서울대학교 대학원

기계항공공학부

김 태 성

음향 가진에 대한 다양한 H<sub>2</sub>/CH<sub>4</sub> 연료 조성의  
Burke-Schumann 화염의 응답 특성

The Response of the Burke-Schumann Flame of H<sub>2</sub>/CH<sub>4</sub>  
fuel to Acoustic Excitations

지도교수 윤 영 빈

이 논문을 공학박사 학위논문으로 제출함

2018 년 8 월

서울대학교 대학원

기계항공공학부

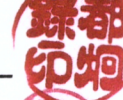
김 태 성


김태성의 공학박사 학위논문을 인준함

2018 년 7 월

위 원 장 : 余載羽 

부위원장 : 尹寧彬 

위 원 : 都炯錄 

위 원 : 金大植 

위 원 : 孫采熏 

## ABSTRACT

The exact mechanism of combustion instability has not yet been elucidated, but it is known that the occurrence of the combustion instability depends on the interaction of the flow perturbation of the reactants, the perturbation of heat release, and the perturbation due to the acoustic boundary of the combustion chamber. If the above three perturbations form a positive feedback loop, the probability of combustion instability increases. Conversely, if a negative feedback loop is formed, the probability of combustion instability is lowered. In order to lower the risk of combustion instability, it is necessary to understand the combustion instability conditions as mentioned above. The basis for understanding the conditions which combustion instability occurs is to study the dynamic characteristics of the flame.

In this study, the dynamic characteristics of Burke-Schumann flame, which is a special case of non-premixed jet flame, composed of a mixture of methane and hydrogen, was studied. The dynamic characteristics of the flame were represented by the perturbation of heat release and flame shape when disturbance was generated from outside. When the flame was at the open boundary, the heat release and the shape of the flame were measured to show the response characteristics of the flame to the external disturbance. When the flame was at the closed boundary, the resonance frequency of the experimental apparatus was obtained and the effect on the resonance frequency was investigated and the cause of the self-excited pressure oscillations was analyzed.

The shape of the flame of the open boundary was three kinds. In the low frequency region, the flame shape was attached to the nozzle in one periodic wave form, and the flame was broken in the above region. In the region near 250 Hz, the flame was hardly shaken. The flame composed of several waves appeared in the remaining region. The flame transfer function also showed a very low value at the point where the flame did not shake and was maintained at a constant value above a certain frequency. The gain of the flame transfer function and the fluctuation of the flame area showed a similar change tendency except for the region where the flame was broken. The flame of the open boundary showed a linear relationship in which the heat release perturbation was approximately proportional to the

velocity perturbation magnitude, but the influence on the 2nd harmonic frequency of the excitation frequency occurred to a large extent. Especially, the ratio of the 2nd harmonic frequency of heat release increased sharply at the excitation frequency or fuel composition, which shows the low gain of the flame transfer function.

At the closed boundary, the influence of the resonance frequency was analyzed. Although the closed boundary was formed by the movable nozzle, since the exhaust duct continued to exist in the longitudinal direction of the combustor, it affected the resonance phenomenon. Therefore, the orifice was installed to minimize the influence of the exhaust duct in the longitudinal direction of the combustor. Two resonant frequencies that can affect the combustion chamber were obtained. The points where these frequencies coincided were identified and the conditions under which the effect of the resonant frequency was likely to be strong were identified. In this case, the point where the effect of the resonance frequency was largest was analyzed by measuring the magnitude of the velocity perturbation. The conditions which the pressure fluctuation occurred in the combustion chamber when there was no external disturbance were identified. The cause of this pressure fluctuation under this condition was analyzed. The conditions of the pressure perturbation coincided with the overlapping conditions between the resonance frequency of the air supply part, the intersection of the resonant frequencies affecting the combustor chamber and the flame transfer function at the open boundary.

It is expected that this study can be used as a preliminary research data for studying the dynamic characteristics of Burke-Schumann flame as well as the mechanism of combustion instability of diffusion flame.

**Keywords:** Combustion Instability, Non-premixed Flame, Diffusion Flame, Jet Flame, Burke-Schumann Flame, Flame Dynamics, Flame Transfer Function, Flame Describing Function, Nonlinear Dynamic Characteristics, Resonant Frequency, Pressure Perturbation, OH-PLIF.

**Student Number:** 2011-20701

# LIST

ABSTRACT .....	i
LIST .....	iii
LIST OF FIGURES.....	v
LIST OF TABLES .....	x
NOMENCLATURE.....	xi
CHAPTER 1	
INTRODUCTION .....	1
CHAPTER 2	
EXPERIMENT AND MEASUREMENT SYSTEMS.....	8
2.1 Combustor and Nozzles.....	8
2.2 Flame Imaging.....	10
2.2.1 Chemiluminescence Spectroscopy.....	10
2.2.2 OH PLIF Measurements .....	12
2.3 Flame Transfer Function Measurement .....	18
CHAPTER 3	
FLAME DYNAMIC CHARACTERISTICS OF BURKE-SCHUMANN FLAME .....	20
3.1 Objectives and Conditions.....	20
3.2 Comparison between Experimental Results and Analytic Results .....	22
3.2.1 Frequency Dependence on the Dynamics of the Flame Surface.....	22
3.2.2 Velocity Dependence on the Dynamics of the Flame Surface .....	28
3.2.3 Dynamics of Heat Release .....	30
3.3 Relation between Heat Release and Flame Area .....	33
3.4 Effect of Velocity and Mass Diffusivity .....	39
3.4.1 Effect on the flame transfer function .....	39

3.4.2 Effect on the flame shape .....	44
3.5 Nonlinear Dynamics .....	48
3.5.1 Flame Describing Function.....	48
3.5.2 Harmonic Flame Transfer Function .....	51
CHAPTER 4	
EFFECT OF CLOSED BOUNDARY ON THE DYNAMICS OF THE BURKE-SCHUMANN FLAME .....	57
4.1 Objectives and Conditions.....	57
4.2 Resonant Frequency of the Combustor.....	59
4.3 Effect of the Combustor Length on Velocity and Heat Release .....	66
4.4 Comparison between Open and Closed Boundary Results .....	73
4.5 Relation with the Combustor Instability Characteristics .....	78
CHAPTER 5	
CONCLUSION.....	83
REFERENCES.....	88
ABSTRACT IN KOREAN.....	92

## LIST OF FIGURES

Fig. 1.1	Schematic of the (a) feedback loop for combustion instability, (b) mechanism from self-excited oscillation to heat release oscillation (ref. [1])	2
Fig. 1.2	Schematic diagram of the 2nd harmonic flame describing function	6
Fig. 2.1	Illustration of the apparatus. (a) Diffusion jet flame burner, (b) Premixed jet flame burner	8
Fig. 2.2	Combustion chamber with a movable nozzle	9
Fig. 2.3	Schematic of energy transfer process. Relaxation processes emission of photons	12
Fig. 2.4	OH excitation spectrum; In this study, $Q_1(6)$ was used for OH PLIF	14
Fig. 2.5	OH fluorescence spectrum for $Q_1(6)$ .	14
Fig. 2.6	Transmittance of bandpass filter	15
Fig. 2.7	Voltage regulation to match the magnitude and phase difference between the velocity perturbation of air and fuel	18
Fig. 3.1	Flame surface with various forcing frequencies using $H_2/CH_4 = 75\%/25\%$ and $u_0 = 1\text{m/s}$ by OH-PLIF	23
Fig. 3.2	Strouhal number dependence of the flame surface using $u_0 = 1\text{ m/s}$ at two different fuel concentration conditions, (a) $H_2/CH_4 = 50\%/50\%$ , (b) $H_2/CH_4 = 75\%/25\%$	23
Fig. 3.3	Frequency dependence of the flame length using $u_0 = 1\text{ m/s}$ at two different fuel concentration conditions	25
Fig. 3.4	Sequence of flame separation with $H_2/CH_4 = 75\%/25\%$ , $u_0 = 1\text{m/s}$ and forcing frequency = 100Hz	26
Fig. 3.5	(a) Flame diameter definition with $U = 1.0\text{ m/s}$ , $u' = 0.25\text{ m/s}$ and $H_2/CH_4 = 75\%/25\%$ , (b) relation between the flame diameter and the velocity perturbation	28



Fig. 3.6	Flame surface with various mean velocities using $H_2/CH_4 = 75\%/25\%$ and forcing frequency = 300 Hz, determined by OH-PLIF	29
Fig. 3.7	Peclet number's (Pe) dependence of the flame surface using $u_0 = 1$ m/s at two different fuel concentration condition, (a) $H_2/CH_4 = 50\%/50\%$ , (b) $H_2/CH_4 = 75\%/25\%$	29
Fig. 3.8	Gain of the flame transfer function of diffusion flame at 1.0 m/s	31
Fig. 3.9	Phase of the flame transfer function of diffusion flames at 1.0 m/s	32
Fig. 3.10	Instantaneous flame surface with various forcing frequencies	34
Fig. 3.11	Partial flame area oscillations and gain of flame transfer function	35
Fig. 3.12	Total and partial flame surface area with 80 Hz forcing frequency	37
Fig. 3.13	Sequence of flame cutting with 80 Hz forcing frequency	37
Fig. 3.14	Flame area perturbation and gain of the flame transfer function with (a) $U = 1.0$ m/s, $H_2/CH_4 = 75\%/25\%$ and $u'/U = 0.1$ , (b) $U = 1.5$ m/s, $H_2/CH_4 = 75\%/25\%$ and $u'/U = 0.1$ , (c) $U = 2.0$ m/s, $H_2/CH_4 = 75\%/25\%$ and $u'/U = 0.1$ , (d) $U = 1.0$ m/s, $H_2/CH_4 = 25\%/75\%$ and $u'/U = 0.1$ , (e) $U = 1.0$ m/s, $H_2/CH_4 = 50\%/50\%$ and $u'/U = 0.1$ and (f) $U = 1.0$ m/s, $H_2/CH_4 = 75\%/25\%$ and $u'/U = 0.1$	38
Fig. 3.15	Flame area perturbation and gain of the flame transfer function with $U = 1.0$ m/s, $H_2/CH_4 = 75\%/25\%$ and (a) $u'/U = 0.1$ , (b) $u'/U = 0.15$ , (c) $u'/U = 0.2$ and (d) $u'/U = 0.25$	39
Fig. 3.16	The flame transfer function with various input mean velocities, (a) gain according to forcing frequency, (b) gain according to Strouhal number	40
Fig. 3.17	The flame transfer function with various input mean velocities, (a) phase according to forcing frequency, and (b) phase according to Strouhal number	41
Fig. 3.18	The flame transfer function with various fuel concentrations, (a) gain according to forcing frequency, (b) gain according to Strouhal number	43
Fig. 3.19	The flame transfer function with various fuel concentrations, (a) phase according to forcing frequency, and (b) phase according to Strouhal	44

	number	
Fig. 3.20	Instantaneous real flame shape at (a) $U = 1.0$ m/s, (b) $U = 1.5$ m/s, (c) $U = 2.0$ m/s with $H_2/CH_4 = 75/25$ , $f = 100$ Hz and (d) $H_2/CH_4 = 75/25$ , (e) $H_2/CH_4 = 50/50$ , (f) $H_2/CH_4 = 25/75$ with $U = 1.0$ m/s, $f = 100$ Hz	45
Fig. 3.21	Instantaneous schematic of flame shape at (a) three different input mean velocities with $H_2/CH_4 = 75/25$ , $f = 100$ Hz and (b) three different fuel concentrations with $U = 1.0$ m/s, $f = 100$ Hz	45
Fig. 3.22	Instantaneous real flame shape at steady state and forced state with one period every 90 degrees with $H_2/CH_4 = 75/25$ , $U = 1.0$ m/s, $u/U = 0.1$ , $f = 100$ Hz	46
Fig. 3.23	Instantaneous schematic diagram of the flame shape at steady state and forced state with one period every 90 degrees with $H_2/CH_4 = 75/25$ , $U = 1.0$ m/s, $u/U = 0.1$ , $f = 100$ Hz	47
Fig. 3.24	Flame transfer function with various velocity perturbation magnitudes according to forcing frequency, (a) gain, (b) phase	49
Fig. 3.25	Instantaneous real flame shape at four different velocity perturbations	50
Fig. 3.26	Instantaneous schematic diagram of the flame shape at four different velocity perturbations	50
Fig. 3.27	Normalized 2nd harmonic response with various fuel composition according to forcing frequency, (a) air velocity, (b) fuel velocity	51
Fig. 3.28	Normalized 2nd harmonic heat release response with various fuel composition according to forcing frequency	52
Fig. 3.29	Normalized 2nd harmonic response with various fuel composition according to forcing frequency, (a) gain of the flame transfer function with air velocity, (b) gain of the flame transfer function with fuel velocity	53
Fig. 3.30	Normalized 2nd harmonic response with various velocity perturbation magnitudes according to forcing frequency, (a) air velocity, (b) fuel velocity	54

Fig. 3.31	Normalized 2nd harmonic heat release response with various velocity perturbations magnitudes according to forcing frequency	55
Fig. 3.32	Normalized 2nd harmonic response with various velocity perturbations magnitudes according to forcing frequency, (a) gain of the flame transfer function with air velocity, (b) gain of the flame transfer function with fuel velocity	56
Fig. 4.1	Temperature distribution calculated by CHEMKIN PRO	60
Fig. 4.2	Resonance frequency up to the movable nozzle and the exhaust duct without orifice condition	65
Fig. 4.3	Resonance frequency up to the movable nozzle and the orifice with orifice condition	65
Fig. 4.4	Standard deviation of the (a) air velocity, (b) fuel velocity and (c) heat release perturbations	68
Fig. 4.5	Maximum variation of (a) air velocity and (b) heat release perturbations with varying the combustor length in the each trend group of air velocity perturbation divided by standard deviation	70
Fig. 4.6	Maximum variation of (a) fuel velocity and (b) heat release perturbations with varying the combustor length in the each trend group of air velocity perturbation divided by standard deviation at the closed boundary without orifice	71
Fig. 4.7	Maximum variation of (a) fuel velocity and (b) heat release perturbations with varying the combustor length in the each trend group of air velocity perturbation divided by standard deviation at the closed boundary with orifice	72
Fig. 4.8	Heat release of open boundary, closed boundary without orifice and closed boundary with orifice by using the flame transfer function concept with 500 mm combustion chamber length	73
Fig. 4.9	Ratio of 1st harmonic velocity and 2nd harmonic velocity of (a) air and (b) fuel with the open boundary, the closed combustor boundary without	74

	orifice and the closed boundary with orifice	
Fig. 4.10	Ratio of 1st harmonic velocity and 2nd harmonic velocity of heat release with the open boundary, the closed combustor boundary without orifice and the closed boundary with orifice	75
Fig. 4.11	2nd harmonic flame transfer function based on the perturbation of the (a) air velocity and (b) fuel velocity by using Eqn. (3)	76
Fig. 4.12	The nonlinearity of the heat release perturbation to the velocity perturbation at the closed boundary without orifice	77
Fig. 4.13	Dynamic pressure in the combustion chamber in the closed boundary combustor with orifice at the (a) 100 mm, (b) 150 mm, (c) 200 mm, (d) 250 mm, (e) 300 mm and (f) 350 mm length of the combustor	79
Fig. 4.14	Dynamic pressure in the combustion chamber in the closed boundary combustor with orifice at the (a) 400 mm, (b) 450 mm, (c) 500 mm, (d) 550 mm, (e) 600 mm length of the combustor	80
Fig. 4.15	Voltage measured by a hot wire anemometer located at the air supply tube with a random frequency	81
Fig. 4.16	Air and fuel velocity perturbation as a function of frequency at the 350 mm length of the combustor with external excitation	82

## LIST OF TABLES

Table 2.1	Formation and destruction of OH radical.	13
Table 2.2	High speed PLIF application research summary	16
Table 3.1	Summary of the test conditions	21
Table 4.1	Summary of the test conditions	58
Table 4.2	Averaged temperature of the combustor	61
Table 4.3	Resonant frequency from bottom of air line to movable nozzle	61
Table 4.4	Resonant frequency from bottom of air line to end of the combustor	62
Table 4.5	Resonant frequency from bottom of air line to end of the combustor with orifice	62
Table 4.6	Resonant frequency from bottom of air line to end of the exhaust duct	63

## NOMENCLATURE

### *Alphabet*

$H$	hydrogen
$O$	Oxygen
$U$	mean velocity
$Pe$	Peclet number
$St$	Strouhal number
$deg$	degree
$n$	gain of the flame transfer function
$u$	velocity
$u'$	velocity perturbation
$\bar{u}$	mean velocity
$q$	heat release
$q'$	heat release perturbation
$\bar{q}$	mean heat release
$w/$	with

### *Greek*

$\omega$	angular frequency
$\Phi$	phase difference or diameter

### *Subscript*

$1st$	1st harmonic
$2nd$	2nd harmonic
$0$	mean
$L_f$	flame length
$d_f$	fuel nozzle diameter

# CHAPTER 1

## INTRODUCTION

Devices that utilize combustion have the risk of combustion instability. It is possible to operate a device by avoiding the instability condition. Moreover, it is possible to install a damping apparatus by predicting instability conditions. Therefore, it is necessary to grasp the condition of the occurrence of combustion instability to avoid a combustion instability occurrence condition or to install a damping apparatus. The precise mechanism of combustion instability has not yet been elucidated. Nonetheless, it is known that the presence or absence of instability depends on the interaction between the flow perturbation, perturbation of the heat release, and the perturbation under the acoustic boundary of the combustion chamber. If the above three perturbations form a positive feedback loop, the probability of combustion instability increases. On the other hand, if a negative feedback loop is formed, the probability of an occurrence of combustion instability is lowered. Therefore, to understand the combustion instability, it is necessary to identify the type of feedback loop constituting the above three factors.

Examination of the feedback process of the three factors reveals the relationship between the flow perturbation and the heat release perturbation. Acoustical effects are then added to the result. For example, the relation between flow perturbation and heat release perturbation is expressed using the flame transfer function or the flame description function. In addition, the sound transfer function or Helmholtz solver is used to add acoustic influence.

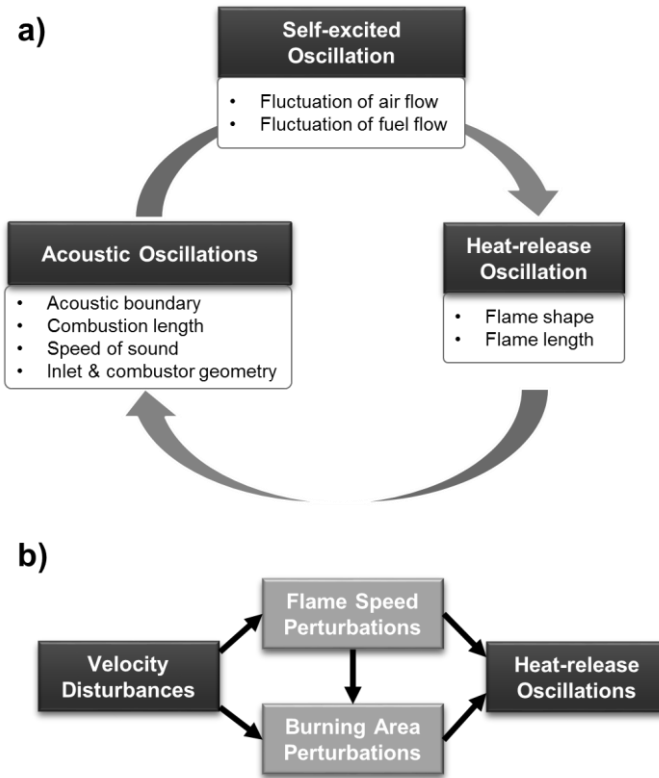


Fig. 1.1 Schematic of the (a) feedback loop for combustion instability, (b) mechanism from self-excited oscillation to heat release oscillation [1]

The relationship between flow perturbation and heat release perturbation is evaluated by theoretical, computational fluid dynamics (CFD), and experimental methods. The flame transfer function shown as Eqn. (1.1) is a function that expresses the rate between the heat release perturbation and the velocity perturbation as a function of frequency by applying the transfer function concept of control engineering to the flame.

$$\text{Flame transfer function} = \frac{q'/\bar{q}}{u'/\bar{u}} = n(\omega) \exp i\phi(\omega) \quad (1.1)$$

The flame transfer function does not consider the absolute magnitude of the velocity



perturbation. Rather, it considers the linear relationship between the velocity perturbation and heat release perturbation. On the other hand, the flame description function shown as Eqn. (1.2), which considers the velocity perturbation as an additional variable in the flame transfer function, has been studied because of the existence of the nonlinear relation velocity perturbation and heat release perturbation.

$$\text{Flame describing function} = \frac{q'/\bar{q}}{u'/\bar{u}} = n(u', \omega) \exp i\phi(u', \omega) \quad (1.2)$$

The flame dynamics of premixed flames have been widely studied by many researchers. For example, S. Ducrix et al. performed a theoretical and experimental study with acoustic forcing to measure the flame transfer function and the flame surface of a conical flame [2]. T. Schuller et al. studied the prediction of the flame transfer function of premixed laminar conical and V flames using the scalar value,  $G$ , to describe the flame front [3]. D. Durox et al. experimentally implemented an inverted conical flame, similar to a V flame to show the flame transfer function. The flame transfer function for various velocity perturbation magnitudes was obtained so that the magnitude of the flame transfer function was influenced by the magnitude of the velocity perturbation. This indicated that the relationship between the heat release oscillations and velocity perturbations is nonlinear [4]. K. Kim et al. studied the response to acoustic velocity and equivalence ratio oscillations for partial flames with experimental methods using the flame transfer function [5]. B. Bellows et al. studied the flame transfer function saturation mechanisms of the swirl-stabilized combustor [6]. W. Polifke et al. studied the flame transfer function low-frequency limit related to the conservation of mass, energy, and momentum [7]. D. Kim et al. measured the flame structure and flame transfer function in a premixed model gas turbine combustor and used experiments to show the relationship between the flame structure and the transfer function [8]. Palies et al. calculated the flame transfer function through  $G$  equation modeling for a premixed flame with a swirl and compared it with the experimental results [9].

N. Noiray et al. confirmed the possibility of predicting the combustion instability with the flame transfer function. The flame transfer function was obtained through experiments with external forcing and theoretical burner acoustics through a premixed flame combustor with a perforated plate on top. The flame transfer function was compared with the self-excited instability by changing the combustor length. To this end, the length the piston was moved to the bottom with the same shape combustor as the combustor used for the flame transfer function measurement. The flame describing function for self-excited instability was calculated, thereby showing that the unstable frequency and velocity vary with the changing length of the resonant cavity [10, 11].

The combustion dynamics of the diffusion flame, by contrast, are less well studied than those of the premixed flame. Analytical studies of diffusion flame dynamics for the Burke-Schumann flame have been presented by K. Balasubramanian et al., who studied the flame response of flow oscillation using the mixture fraction equation known as the Z-equation [12, 13]. The Burke-Schumann flame is the special case of the diffusion jet flame with coaxial air. This flame model shows consists of the basic properties of diffusion. This model involves the streamwise convection and the transverse diffusion balance. The Burke-Schumann flame is shown by the mixture fraction equation named as the Z-equation with two main assumptions. First assumption is that the transverse convection and the streamwise diffusion are neglected. Second assumption shows the limitation of this flame. This flame model has high accuracy with the optimum level of the Peclet number. Similar to G-equation in premixed flame, the dynamic of the Burke-Schumann flame is described by the solution of the Z-equation with infinitely fast chemistry. The flame sheet is described by the stoichiometric mixture fraction surface,  $Z_0$ . The flame surface calculated by the Z-equation solution is used to calculate the heat release. N. Magina et al. studied the flame dynamics of the Burke-Schumann flame and compared the dynamics of diffusion flames with those of premixed flames [14, 15, 16]. N. Magina et al. obtained the flame transfer function through the Z equation for the Burke-Schumann flame and compared it with the results of the premixed flame. The change of flame shape, flame transfer function, and flame position near the nozzle were shown by the theoretical method with the variation of

the Péclet number. Z. Yao et al. studied the flame shape and distributed flame transfer function and compared the analytical results using Green's function method with CFD calculations [17]. Farhat et al. generated a perturbation in the combustion chamber through the speaker where the jet diffusion flame is formed, and they measured the fluctuation of the flow rate and flame [18]. Wang et al. experimentally studied the flame shape and frequency of the flame fluctuation when a low frequency velocity perturbation exists in the fuel with a bluff-body nozzle. The correlation between the flickering frequency and velocity perturbation frequency of the flame was investigated. The lifted flame phenomenon was also measured when there was no excitation [19].

The Flame describing function is to investigate the nonlinear characteristics of the flame by adding the magnitude of the velocity perturbation to the flame transfer function. However, since the flame describing function is basically an extension of the flame transfer function, it contains only the flame response to the input forcing frequency. The thermoacoustic phenomenon affected by the resonance frequency of the combustion chamber occurs not only at the first harmonic frequency of the resonance frequency but also at higher harmonic frequencies such as 2nd and 3rd harmonic frequency. This higher harmonic phenomenon was found in the combustion instability. T. Lieuwen theoretically analyzed the effect of higher harmonic frequencies [20]. K. Kim and J. Yoon et al. analyzed experimentally high harmonic combustion instability in model gas turbine combustors [21, 22]. For this phenomenon, A. Orchini et al. proposed a flame describing function with a double input to account for harmonic velocity fluctuations [23]. The flame describing function considering the 2nd harmonic fluctuation is composed as shown in Fig. 1-1, and expressed as Eqn. (1.3). The 1st flame describing function shows the relation between the velocity oscillations and heat release perturbation with the same oscillating frequency. The 2nd flame describing function shows the relation between the heat release perturbation and the velocity oscillation when the heat release is oscillated with twice the frequency of the velocity oscillation.

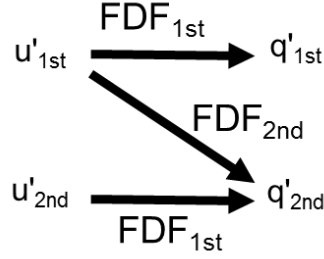


Fig. 1.2 Schematic diagram of the 2nd harmonic flame describing function

$$FDF_{2nd}(u', \omega) = \frac{q'_{2nd}}{u'_{1st}} - FDF_{1st}(u', 2\omega) \frac{u'_{2nd}}{u'_{1st}} \quad (1.3)$$

The combustion instability phenomenon is likely to occur when the heat release oscillation caused by the flow perturbation is influenced by the length, shape, and acoustical boundary of the combustor to amplify the pressure perturbation and this pressure perturbation amplifies the flow perturbation again as shown in Fig. 1-1(a). Therefore, it is necessary to form an acoustical boundary in order to simulate the combustion instability phenomenon. In addition, the resonance frequency formed inside the combustion chamber varies depending on where the acoustic boundary is formed. Therefore, in order to link flame dynamic characteristics with the combustion instability, a device capable of varying the length of the combustor so that various resonance frequencies can be formed in the combustion chamber is needed. M. Kim et al. experimentally showed the degree of the combustion instability depending on the combustor length, flow velocity, and equivalence ratio in the model gas turbine combustor [24].

The purpose of this study was to investigate the flame dynamics and combustion instability of Burke-Schumann flame experimentally. Several studies have been carried out on the flame dynamics of the Burke-Schumann flame, but most are limited to theoretical results and few experimental studies have been conducted. The flame dynamics study is a study to understand the combustion instability phenomenon, but the study on the combustion instability of the Burke-Schumann flame has hardly progressed despite the

study of the flame dynamics. Therefore, in this study, the flame dynamics of Burke-Schumann flame was experimentally measured and correlated with the flame dynamics characteristics and the combustion instability.

In summary, the objective of this study is to identify the linear and nonlinear dynamics of the Burke-Schumann flame and to investigate the effects on the dynamic characteristics and the combustion instability when acoustical boundaries were formed. For these purposes, the following studies were performed.

1. In Chapter 3, the flame transfer function of the Burke-Schumann flame was measured and the flame shape was measured using high speed PLIF technique. These results were compared with the theoretical results. The effect of flame area perturbations on the heat release perturbations shown in Fig.1-1(b) was investigated. The dynamic characteristics of this flame for various flow rates and fuel compositions were determined. The nonlinear dynamics of the Burke-Schumann flame were investigated using the flame describing function and the harmonic flame transfer function.
2. In Chapter 4, the effects of the combustor boundary on the dynamic characteristics of this flame and the combustion instability were investigated. The dynamic characteristics of this flame were compared under the same conditions except for the presence of the combustor boundary. When the length of the combustor was changed, the change of flow was identified. In addition, the conditions of the combustion instability were related to the dynamic characteristics of the flame.

## CHAPTER 2

### EXPERIMENT AND MEASUREMENT SYSTEMS

#### 2.1 Combustor and Nozzles

A non-premixed jet flame combustor was designed for this study to test the Burke-Schumann flame. As shown in Fig. 2.1, this combustor consists of a fuel supply line with a 5 mm inner diameter and an air supply line with a 50 mm inner diameter. A square quartz tube is installed at the top of air nozzle to visualize the flame.

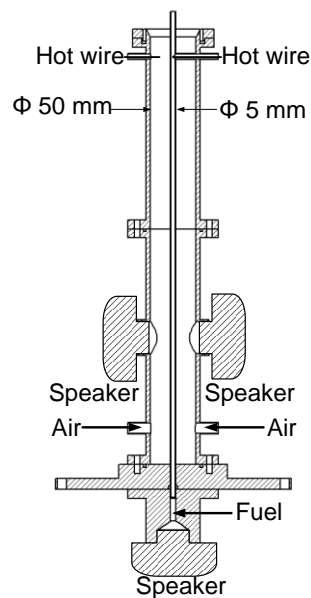


Fig. 2.1 Illustration of the diffusion jet flame burner

To analyze the effect of the closed boundary, the piston was mounted on the top of the combustor to change the combustor length. It could be moved from 0 mm to 620 mm as shown in Fig. 2.2. Eight dynamic pressure sensors were mounted on one side of the wall with 55-mm intervals for dynamic pressure measurement.

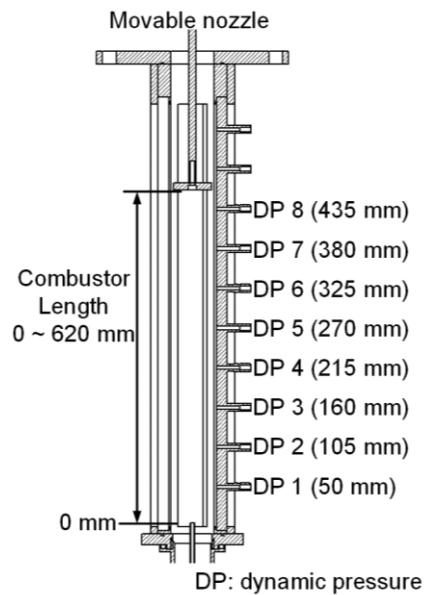


Fig. 2.2 Combustion chamber with a movable nozzle

The fuel used in this study was a mixture of hydrogen and methane. When the inner diameter ratio of the combustor between the air and fuel is 10, the Burke-Schumann flame with pure methane is in an unstable state and is quickly extinguished. In contrast, a pure hydrogen flame is so stable that the flame cannot oscillate with external forcing. Therefore, a mixture of hydrogen and methane is a suitable fuel because the Burke-Schumann flame with this mixture is attached at the tip of the nozzle without forcing and shows an adequate flame oscillation.

The mass flow controllers were adapted to supply both fuel and air to the combustor at the same velocity. The hydrogen, methane, and air are supplied by each mass flow controller.

The flow perturbation is generated by three loudspeakers: one loudspeaker is installed at the bottom of the fuel line and the other two are located beside the air feeding line. In this condition, the phase and velocity difference in perturbation between air and fuel is limited to 5 degrees and 0.05 m/s using the trial-and-error method.

## 2.2 Flame Imaging

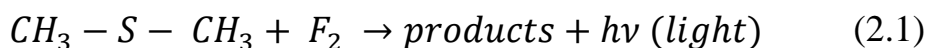
In this study, OH\* chemiluminescence images were recorded to measure flame length and flame structure. Many other studies used direct photography to identify flame structure; however, images produced by this method are not good indicators of the reaction zone. The OH\* chemiluminescence image should be used since OH radicals are good indicators of the reaction zone, which is a high temperature region. Thus, OH\* images were acquired using an intensifier (Highspeed IRO, LaVision) and CMOS camera (Highspeed Star 8, LaVision, 1024 x 1024 pixel) with a UV imaging lens ( $f = 100$  mm;  $f/2.8$ ) and  $320 \pm 20$  nm narrow bandpass filter. OH\* images were taken with 1 ms exposure time and 7000 images per second.

### 2.2.1. Chemiluminescence Spectroscopy

Chemiluminescence, like atomic emission spectroscopy (AES), uses quantitative measurements of the optical emission from excited chemical species to determine analyte concentration; however, unlike AES, chemiluminescence is usually emission from energized molecules instead of simply excited atoms. The bands of light determined by this technique emanate from molecular emissions and are therefore broader and more complex than bands originating from atomic spectra. Furthermore, chemiluminescence can take place in either the solution or gas phase, whereas AES is almost strictly as gas phase phenomenon. Like fluorescence spectroscopy, chemiluminescence's strength lies in the detection of electromagnetic radiation produced in a system with very low background. And on top of this, because the energy necessary to excite the analytes to higher electronic, vibrational, and rotational states (from which they can decay by emission) does not come from an external light source like a laser or lamp, the problem of excitation source scattering is completely avoided. The major limitation to the detection limits achievable by chemiluminescence involves the dark current of the photomultiplier (PMT) necessary to detect the analyte light emissions. If the excitation energy for analytes in chemiluminescence doesn't come from a source lamp or laser, where does it come from?



The energy is produced by a chemical reaction of the analyte and a reagent. An example of a reaction of this sort is shown below:



In gas phase chemiluminescence, the light emission (represented as  $h\nu$ ) is produced by the reaction of an analyte (dimethyl sulfide in the above example) and a strongly oxidizing reagent gas such as fluorine (in the example above) or ozone, for instance. The reaction occurs on a time scale such that the production of light is essentially instantaneous; therefore, most analytical systems simply mix analytes and the reagent in a small volume chamber directly in front of a PMT. If the analytes are eluting from a gas chromatographic column then the end of the column is often fed directly into the reaction chamber itself. Since as much of the energy released by the reaction should (in the analyst's eye) be used to excite as many of the analyte molecules as possible, loss of energy via gas phase collisions is undesirable, and therefore a final consideration is that the gas pressure in the reaction chamber be maintained at a low pressure ( $\sim 1$  torr) by a vacuum pump in order to minimize the effects of collisional deactivation. It must be stated that the ambiguous specification of "products" in the above reaction is often necessary because of the nature and complexity of the reaction. In some reactions, the chemiluminescent emitters are relatively well known. In the above reaction the major emitter is electronically and vibrationally excited HF; however, in the same reaction, other emitters have been determined whose identities are not known and these also contribute to the total light detected by the PMT. To the analytical chemist the ambiguity about the actual products in the reaction is, in most case, not important. All the analyst cares about is the sensitivity of the instrument (read detection limits for target analytes), its selectivity-that is, response for an analyte as compared to an interfering compound, and the linear range of response. In chapter 3 and 4, OH\* chemiluminescence measurements were conducted to obtain the reaction region. Finally, we could obtain the flame lengths based on the radical (OH radical in this study) by high UV quantum efficiency ICCD camera rather than the visible flame

length based on the visible mixed emissions by normal SLR camera.

### 2.2.2. OH PLIF Measurement

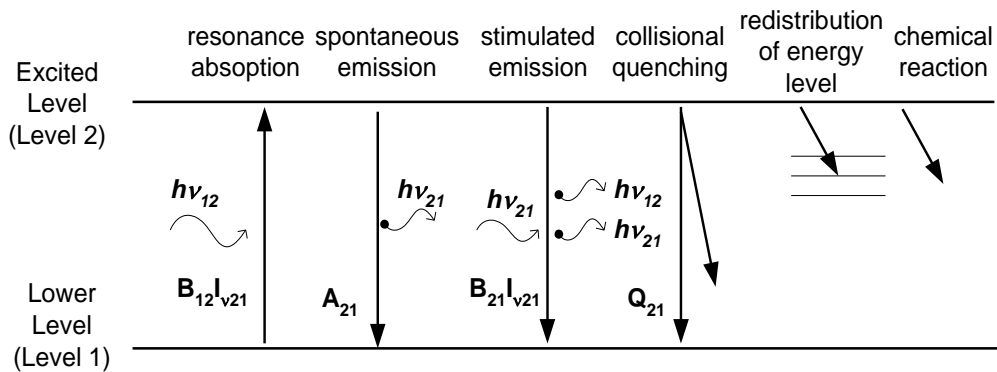


Fig. 2.3 Schematic of energy transfer process. Relaxation processes emission of photons

Laser induced fluorescence (LIF) is described as the absorption of a photon by a molecule of radical, followed by an emission of a photon as the molecules undergoes the transition from a higher level energy state to a lower one. Figure 2.3 shows the schematic of energy transfer process. Some of the molecules will relax to the initial state by emission of photon. Several relaxation processes are possible including (a) spontaneous emission, (b) stimulated emission by exterior stimulus, (c) quenching by collision of molecules, (d) redistribution of energy level, and (e) change of molecular component by chemical reaction. However, the rapid or spontaneous emissions of photons are termed as LIF. The frequency of LIF signal can have different value from that of inducing laser beam.

OH PLIF was used to obtain spatially and temporally resolved images of the reaction zone in various combustors. As described in Table 2.1, the OH radical concentration increases rapidly around the flame in about 20  $\mu$ sec and then decomposes slowly in 1 to 5 ms by a 3-body recombination reaction [25]. Thus, near the flame front exists super-equilibrium OH. The OH radical, which is intermediate product of chemical reaction, has a concentration of more ten times than that of O or H radicals [26]. Therefore, the OH radical is found to emit more intensive fluorescence signal than other species when

absorbing laser light. Hence, the fluorescence signal of OH radical is widely used as an indicator of flame front in reacting flows.

Table 2.1 Formation and destruction of OH radical.

Fast OH formation by two-body reactions (1~5nsec)
$H + O_2 \leftrightarrow OH + O$
$O + H_2 \leftrightarrow OH + H$
$H + HO_2 \leftrightarrow OH + OH$
Slow destruction by three-body recombination reactions (~20μsec)
$H + OH + M \leftrightarrow H_2O + M$

OH PLIF was used to obtain spatially and temporally resolved images of the reaction zone in various combustors. As described in Table 2.1, the OH radical concentration increases rapidly around the flame in about 20 μsec and then decomposes slowly in 1 to 5 ms by a 3-body recombination reaction [30]. Thus, near the flame front exists super-equilibrium OH. The OH radical, which is intermediate product of chemical reaction, has a concentration of more ten times than that of O or H radicals [31]. Therefore, the OH radical is found to emit more intensive fluorescence signal than other species when absorbing laser light. Hence, the fluorescence signal of OH radical is widely used as an indicator of flame front in reacting flows.

To observe the line positions for transition, we scanned the dye laser and recorded the signal at each step. We intended to use Q1(6) transition of the  $A_2\Sigma^+ \leftarrow X_2\Pi$  ( $v' = 1, v'' = 1$ ) band ( $\lambda = 282.94$  nm) for the excitation wavelength and to collect the fluorescence signal from the A-X (1, 0) and (0, 0) bands ( $\lambda = 306 \sim 320$  nm). Using monochromator and PMT (photo-multiplier tube), in conjunction with a test flame in laminar premixed condition, a laser excitation scan was performed over the range of interest from  $\lambda = 282.5$  nm to  $\lambda = 283.5$  nm with 0.001 nm step. The monochromator was fixed at 315 nm to collect

the fluorescence. The signal was multiplied by PMT and recorded through the boxcar averager. At every scanning step, 10 pulses of signal were recorded and averaged. After scanning the dye laser, the OH excitation spectrum can be obtained as shown in Fig 2.4. Among the peak values of excitation spectrum, we used Q1(6) as the excitation wavelength of OH radical.

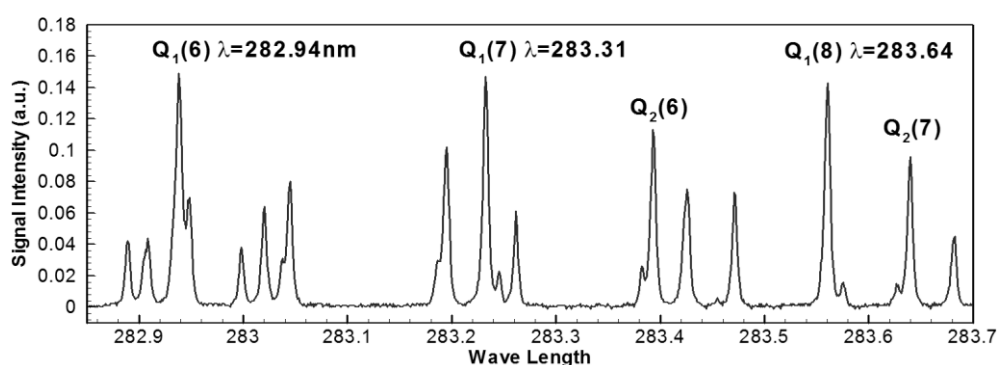


Fig. 2.4 OH excitation spectrum; In this study, Q<sub>1</sub>(6) was used for OH PLIF.

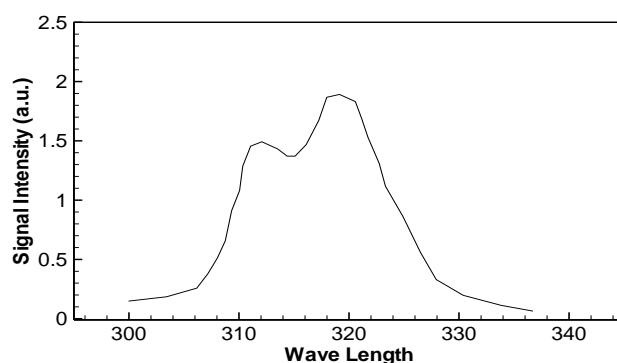


Fig. 2.5 OH fluorescence spectrum for Q<sub>1</sub>(6).

When the location of Q1(6) line was detected, the fluorescence spectrum could be obtained by recording the LIF signal at each scanning step of the monochromator. Figure 2.5 is OH fluorescence spectrum graph for Q1(6). Peak value is found at 320nm.

## PLIF System

For OH PLIF, an Nd:YAG pumped dye laser was turned to Q1(6) transition of the  $A2\Sigma^+ \leftarrow X2\Pi$  ( $v' = 1, v'' = 1$ ) band ( $\lambda = 282.94$  nm). Q1(6) transition line is generally used in the measurement of molecular concentration because it has large LIF signal and the dependency for temperature is low. Fluorescence from the A-X (1, 0) and (0, 0) bands ( $\lambda = 306 \sim 320$  nm) were collected with a UV lens 100 mm/f 2.8 objective. Because UV light cannot penetrate the common glass, all the lenses should be made with quartz. The region of interest was focused onto the intensifier and CMOS camera of LaVision. Advanced bandpass filters were used to block scattered signal lights. Transmittance of filter is shown in Fig. 2.6.

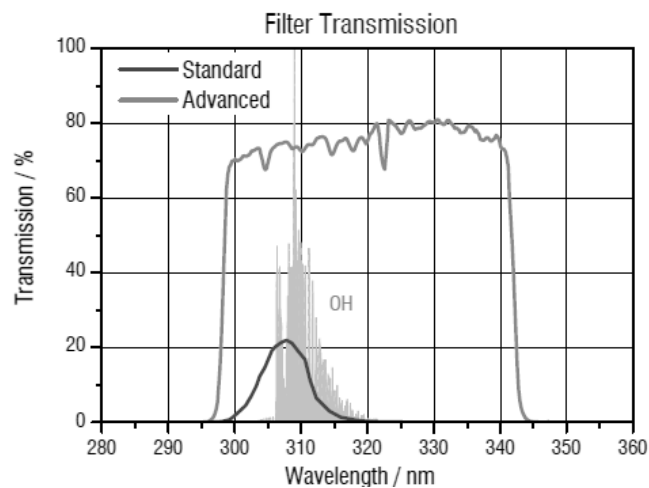


Fig. 2.6 Transmittance of bandpass filter

## High speed PLIF System

High speed laser measurement widely applied in various research field to find the unknown characteristics of high frequency phenomenon. Many research groups are conducting experimental approach about CH<sub>4</sub>/Air flame, Liquid fuel flame and micro structure of the flame. The detailed information about the research are summarized in Table.

## 2.2.

Table 2.2 High speed PLIF application research summary

<b>Research Group</b>	<b>Year</b>	<b>Author</b>	<b>Contents</b>	<b>Rep. Rate</b>
<b>DLR</b>	2013	M. Stohr	Simultaneous measurement of PIV & OH PLIF in CH <sub>4</sub> swirling flame [27]	10 kHz
<b>DLR</b>	2011	M. Stohr	Blow off characteristics of CH <sub>4</sub> swirling flame [28]	5 kHz
<b>DLR</b>	2010	I. Boxx	Simultaneous measurement of transient phenomena in a partially premixed swirl flame [29]	5 kHz
<b>CNRS</b>	2012	P. Petersson	Simultaneous high-speed PIV & OH-PLIF about coaxial diffusion flame burner [30]	10 kHz
<b>CNRS</b>	2014	P. Xavier	Cavity flame anchoring characteristics based on high-speed OH-PLIF [31]	10 kHz
<b>University of Cambridge</b>	2011	J. R. Dawson	Near blow-off characteristics of bluff body stabilized CH <sub>4</sub> flame [32]	5 kHz
<b>University of Cambridge</b>	2012	N. A. Worth	Flame interaction of CH <sub>4</sub> /air conical bluff-body stabilized flame [33]	5 kHz
<b>AFRL</b>	2013	S. Hammack	Plasma-enhanced flame characteristics of turbulent non-premixed flame [34]	10 kHz
<b>Michigan University</b>	2015	P.M. Allison	CH <sub>2</sub> O-PLIF measurements in dual-swirl burner [35]	4 kHz
<b>Sydney University</b>	2011	S. Meares	High-speed OH-PLIF imaging of extinction and re-ignition [36]	5 kHz

In this study, the effect of the high frequency excitation were measured and the application of high speed OH-PLIF in necessary to find the high frequency structural characteristics. High speed OH-PLIF were set up at the rate of 7 kHz. The 7 kHz OH-PLIF used the laser beam from an Nd-YAG laser (Edgewave, IS-200-L) as the pumping source for the dye laser (Sirah, Credo-Dye-LG-24) and the OH fluorescence signal was measured by an intensifier (Hightspeed IRO), a high speed camera (Hightspeed star 8), a UV lens (f/2.8) and a bandpass filter ( $320\pm 20$  nm).

## 2.3 Flame Transfer Function Measurement

The velocity oscillations and heat release rate oscillations are measured to calculate the flame transfer function. The velocity is measured using a hot wire anemometer. The hot wire anemometer is located at the same position of the air and fuel supply lines. The heat release is measured using the photomultiplier tube with a bandpass filter that passes through the OH radical. Heat release measurement was performed by a Hamamatsu photomultiplier tube with WG305 and UG11 filters to measure the intensity of the OH chemiluminescence. The velocity perturbation was measured by the MiniCTA of Dantec Dynamics on the fuel and air nozzles. The voltage measurement for the velocity and heat release signal was performed by using a National Instruments CompactDAQ. The device for applying voltage to the speaker was a function generator, FG420, from Yokogawa. The velocity and heat release rate are measured simultaneously using a data acquisition board with a 10 kHz sampling rate.

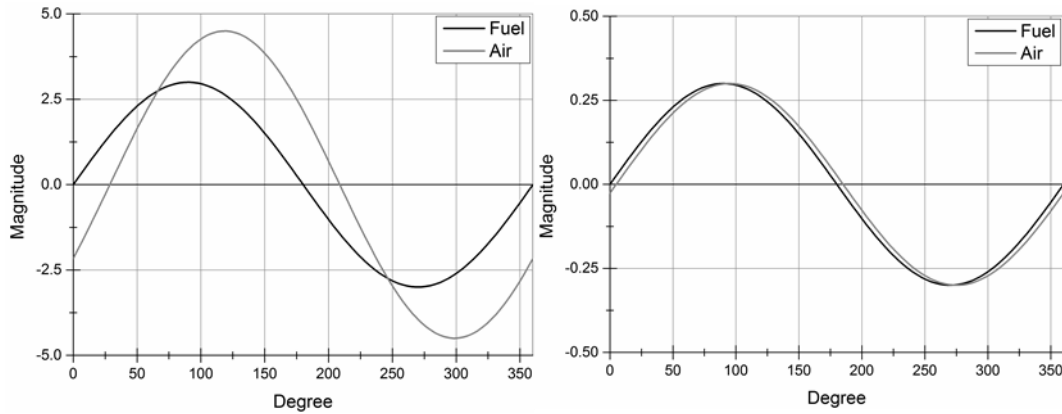


Fig. 2.7 Voltage regulation to match the magnitude and phase difference between the velocity perturbation of air and fuel

Speakers were used to generate velocity perturbations in air and fuel. Two loudspeakers were installed on the left and right sides of the air pipe, and one speaker was attached to



the bottom of the fuel pipe. To simulate the Burke–Schumann flame structure, the velocity and air velocity fluctuations of the air and fuel had to be equal in magnitude and phase. Thus, the trial-and-error method was used to control the voltage applied to the speakers. Through this voltage regulation, the magnitude and phase difference between the velocity perturbation of air and fuel was lower than 0.03 m/s and 10 degrees as shown in Fig.2.7. Therefore, the velocity perturbation is almost constant regardless of the forcing frequency.

## **CHAPTER 3**

# **FLAME DYNAMIC CHARACTERISTICS OF BURKE-SCHUMANN FLAME**

### **3.1 Objectives and Conditions**

This study focused on the dynamic characteristics of the Burke-Schumann flame. This study was motivated by the analytical studies of the dynamics of diffusion flames. The experimental dynamic characteristics of diffusion flames have rarely been studied.

Therefore, this study has focused on the experimental study of the characteristics of diffusion flame dynamics. The goal was to investigate the Burke-Schumann flame, which is a special case of a non-premixed jet flame with coaxial air. In this study, both the air and the fuel had external forcing of the same magnitude and phase to satisfy the conditions of the Burke-Schumann flame. This study measured the flame surface oscillations and the heat release rate oscillations and then compared the measurements with the analytical solution of the Burke-Schumann flame.

Accordingly, the dependence of the Péclet number on the dynamic characteristics of the Burke-Schumann flame in the theoretical studies was experimentally confirmed. The Péclet number—a group of non-dimensional numbers using the mass diffusion coefficient, flow velocity, and fuel nozzle diameter—is considered a single variable in analytical studies. This study compared the changes in dynamic characteristics of the various Péclet numbers. They varied the mass diffusivity and changes in the dynamic characteristics of the various Péclet number while varying the flow velocity.

In addition, the nonlinear characteristics of flame dynamics were investigated. In the early days of the flame dynamic characteristics study, the linear dynamic characteristics such as the flame transfer function proceeded. However, many researchers have confirmed that there is a nonlinear section in the actual phenomenon, and this study also tried to compare the nonlinear characteristics of the Burke-Schumann flame with the linear

characteristics.

To compare between the analytical results and the experimental data, the Burke-Schumann flame uses a mixture ratio of fuel defined as 75% hydrogen and 25% methane or 50% hydrogen and 50% methane. The velocities of the fuel and air are the same and are controlled from 1.0 m/s to 2.5 m/s in 0.5 m/s steps. The fuel of the premixed flame uses a mixture that was determined to be 50% hydrogen and 50% methane because of the potential for flashback with 75% hydrogen and 25% methane under experimental conditions. The flame length and flame transfer function are measured for the premixed flame when the equivalence ratio is controlled as 1 and the velocity of the reactants is 1 m/s.

Table 3.1 Summary of the test conditions

<b>Parameters</b>	<b>Comparison between experiments and analytics</b>	<b>Effect of velocity and fuel composition</b>	<b>Nonlinear Dynamics</b>	<b>unit</b>
<b>Fuel composition</b>	75/25, 50/50	75/25, 50/50, 25/75	75/25, 50/50, 25/75	H <sub>2</sub> [%]/CH <sub>4</sub> [%]
<b>Flow velocity</b>	1.0, 1.5, 2.0, 2.5	1.0, 1.5, 2.0	1.0	m/s
<b>Reynolds number (air)</b>	1,457 ~ 3,642	1,457 ~ 2,913	1,457	-
<b>Reynolds number (fuel)</b>	99 ~ 451	99 ~ 404	99 ~ 202	-
<b>Velocity perturbation</b>	0.2	0.1,	0.1, 0.15, 0.2, 0.25	m/s
<b>Forcing Frequency</b>	80 ~ 400			Hz

To analyze the effect of the Péclet number, Péclet number increased with the decreasing mass diffusion coefficient by increasing the methane rate in the fuel composition from 25% to 75%, and by increasing the average velocity of the input flow from 1.0 m/s to 2.0 m/s. In addition, the effect of the velocity perturbation magnitude was investigated by increasing the magnitude of the velocity perturbation from 0.1 m/s to 0.25 m/s.

The flame surface measurement is performed with the LIF system with a 7 kHz repetition rate and 1024×1024 resolution when the external forcing frequency ranges from 100 Hz to 300 Hz per 50 Hz. The flame length is measured using a DSLR camera, with an exposure time of 10 seconds, which gives a flame length with forcing averaged over 10 seconds.

The flame structure and heat release were measured by using OH chemiluminescence. For the flame measurement, 7,000 images per second were captured at a 1024×1024 resolution with a Highspeed IRO, HighSpeedStar 8, 100 mm focal length UV lens and filter for OH imaging manufactured by LaVision.

The experiments to measure the flame length and flame transfer function are performed from 20 Hz to 400 Hz at 20 Hz steps.

## **3.2 Comparison between Experimental Results and Analytic**

### **Results**

#### 3.2.1. Frequency dependence on the dynamics of the flame surface

The flame surface and length are measured with various external forces, from 100 Hz to 300 Hz in 50 Hz steps, and with input mean velocities from 1.0 m/s to 2.5 m/s in 0.5 m/s steps, using LIF techniques. The flame surface of one case of the test condition that was varied by the forcing frequency is shown in Fig. 3.1. The position of the instantaneous flame surface in the axial direction is described by the Strouhal number of the flame length ( $St_{L_f} = f L_f / u_0$ ), which consists of the forcing frequency, flame length, and flow velocity without forcing ( $u_0$ ), as shown in Fig. 3.2.

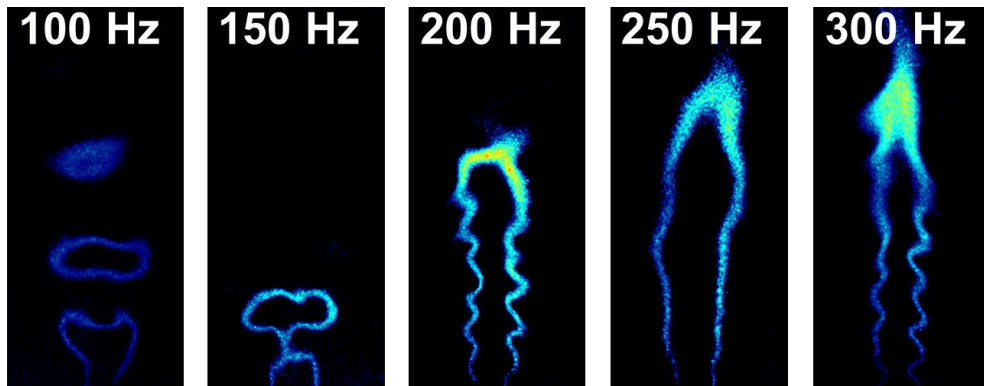


Fig. 3.1 Flame surface with various forcing frequencies using  $H_2/CH_4 = 75\%/25\%$  and  $u_0 = 1\text{m/s}$  by OH-PLIF

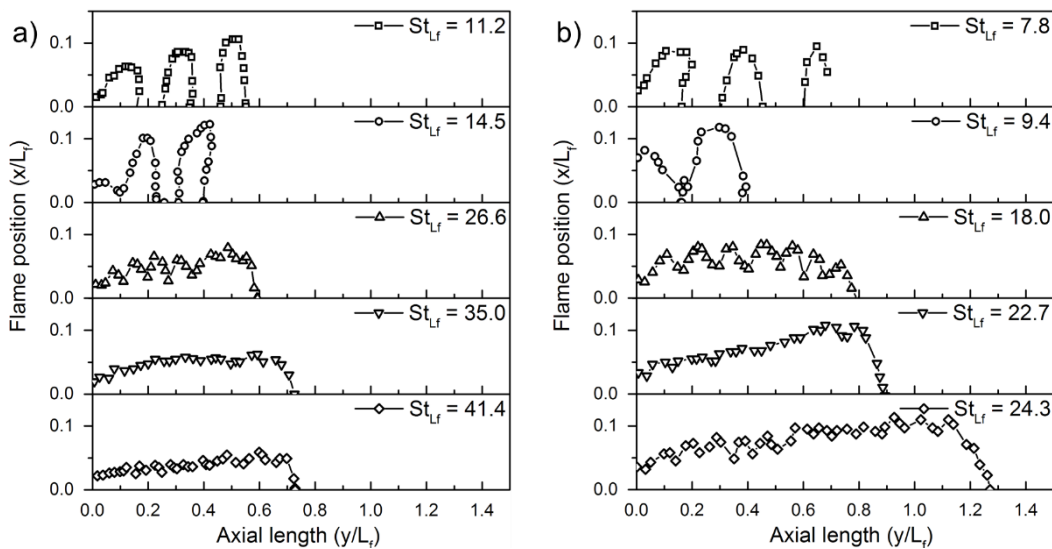


Fig. 3.2 Strouhal number dependence of the flame surface using  $u_0 = 1\text{ m/s}$  at two different fuel concentration conditions, (a)  $H_2/CH_4 = 50\%/50\%$ , (b)  $H_2/CH_4 = 75\%/25\%$

When the Strouhal number is low because of a low forcing frequency, the flame surface consists of one or two periods of undulation. The flame surface consists of several undulations as the Strouhal number increases, except for a Strouhal number with a force of 250 Hz. However, the correlation between flame shape and the magnitude of the Strouhal

number is weak. The flame surface shape is related to the forcing frequency. Nevertheless, the flame surface is shown with the Strouhal number because of the comparison with the analytical solution.

The presence of external forcing shortens the flame length, but this length increases with an increasing forcing frequency. M. Kim et al. reported that the mixing that occurs between air and fuel is enhanced by acoustic forcing in the non-premixed jet flame and showed that this enhancement was greatly increased with resonant frequency forcing [37].

The flame length decreases with acoustic forcing because of the enhanced degree of mixing. The dotted lines in Fig. 3.3 are the flame length without external forcing. The flame length without forcing is 148 mm at 50% hydrogen and 50% methane and 90 mm at 75% hydrogen and 25% methane. When the forcing frequency is 100 Hz, the flame length is 17.5 mm at a 50%/50% fuel concentration and 12.5 mm with a 75%/25% fuel concentration. The flame length decreases until 160 Hz of forcing. The flame length increases from 160 Hz to 200 Hz. When the forcing frequency is larger than 200 Hz, the flame length is nearly constant, as shown in Fig. 3.3.

The resonant frequencies are calculated using COMSOL Multiphysics. The resonant frequency of the fuel line is 137 Hz with the 50%/50% flame and 178 Hz with the 75%/25% flame. The resonant frequency of the air line is 160 Hz. When the resonant frequency of the air line changes from 160 Hz to 199 Hz because the speaker located in the air line is changed, the flame-cutting phenomenon does not occur at 160 Hz. When the resonant frequency of the air line is changed, the flame-cutting phenomenon occurs below 140 Hz of forcing. The excitation frequency when the flame length is the minimum is the same regardless of changing the fuel concentration that makes the resonant frequency of the fuel line change. Therefore, the flame cutting phenomenon and length are related to the resonant frequency of the air line.

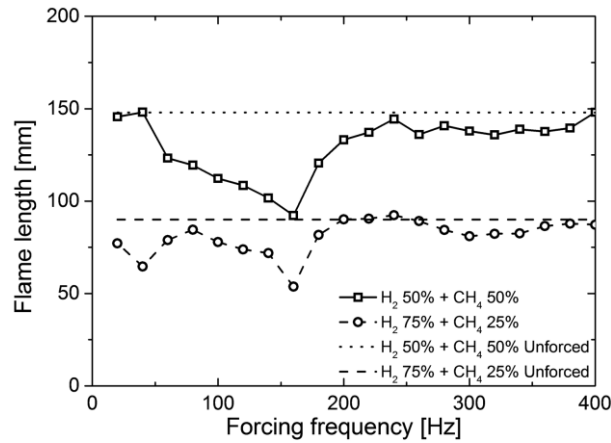


Fig. 3.3 Frequency dependence of the flame length using  $u_0 = 1$  m/s at two different fuel concentration conditions

The fuel consisting of 50% methane and 50% hydrogen tends to show a greater reduction in the flame length. The test conditions of the two experiments shown in Fig. 4 are nearly identical, except for the fuel concentration that determines the mass diffusivity, which is calculated by the equation of the diffusion coefficient in a binary mixture described in C. Wilke et al.'s study [38]. Therefore, the forcing effect on the flame length is larger when the mass diffusivity is low.

The oscillation tendency of the flame surface is divided into three categories, according to the forcing frequency, as shown in Fig. 3.2. At first, when the forcing frequency is 100 and 150 Hz, which are shown in the first and second graphs in Fig. 3.2, a local stagnation of the flame and the flame-cutting phenomenon are seen once every cycle. Figure 3.4 shows the local stagnation of the flame propagation and the flame cutting in a specific condition. The stagnation point of the flame appears at the instant the flame is cut. The flame assumes a heart shape because of this stagnation.

It is possible to consider fuel and coaxial air as the pulsed flow of a single nozzle because the magnitude of velocity perturbation and the phase of both fuel and air are same. The pulsed jet flow is described by K. Lakshminarasimhan [39]. The suction phase of the pulsed non-reaction jet is divided into two direction flows. The flow below the stagnation

point reverses into the nozzle, and the flow above the stagnation point moves upward.

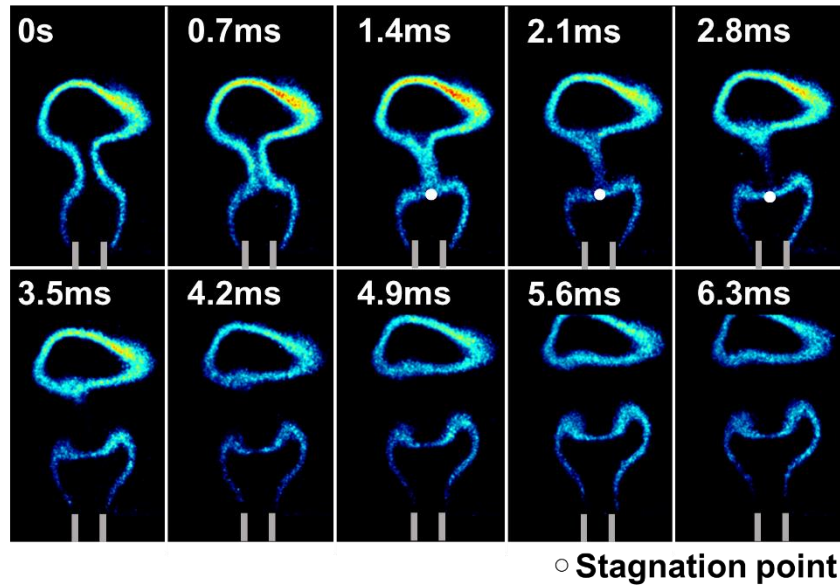


Fig. 3.4 Sequence of flame separation with  $\text{H}_2/\text{CH}_4 = 75\%/25\%$ ,  $u_0 = 1\text{m/s}$  and forcing frequency = 100 Hz

Figure 3.4 shows the stagnation point of the flame. The flame surface located in the upper region above the stagnation point appears along the vertical structure. The flame surface located near the nozzle changes from a convex shape to a concave shape. These phenomena are similar to the 13th figure in the 15th reference, but the reverse flow is temporary above the nozzle. When the flame-cutting phenomenon occurs, the velocity perturbation measured by the hot wire probe always has a positive value. Thus, the reverse flow at the flow line does not exist.

Unburnt gas cannot be supplied to the reaction zone because the flow is stagnant. Therefore, the flame is cut just above the stagnation point. The excitation with 200 Hz of forcing has a shorter suction phase than 100 Hz and 150 Hz of forcing. Thus, the suction phase time is insufficient for cutting the flame when the forcing frequency is higher than 200 Hz.



The condition occurring the flame cutting phenomenon varies with mean velocity, fuel concentration and velocity perturbation. When the fuel concentration is 75% hydrogen and 25% methane and the ratio of the velocity perturbation and the mean velocity is 0.1, the flame is cut at 80 Hz or below forcing with the 1.0 m/s of the mean velocity. But, flame does not cut at the forcing frequencies of the experimental conditions with the 1.5 m/s and 2.0 m/s of the mean velocity. When the mean velocity is 1.0 m/s and the ratio of the velocity perturbation and the mean velocity is 0.1, the flame is cut at 80 Hz or below forcing with the 75% hydrogen and 25% methane. But, flame does not cut at the fuel concentration of the experimental conditions. When the fuel concentration is 75% hydrogen and 25% methane and the mean velocity is 1.0 m/s, the flame is cut with 80 Hz with the 0.1 m/s velocity perturbation, 100 Hz with the 0.1 m/s and 0.2 m/s perturbation, 120 Hz with the 0.25 m/s and 140 Hz with the 0.3 m/s perturbation. Therefore, the flame cutting phenomenon is affected by the mean velocity, fuel concentration and velocity perturbation. The mean velocity and mass diffusivity affect the flame length. The magnitude of the velocity perturbation affect the oscillation degree of the flame. The flame cutting phenomenon is a combination of the axial and radial flow progress.

The flame diameter is defined to calculate the oscillation degree of the flame. Figure 3.5 shows the flame diameter expressing the flame oscillation degree and the relation between the velocity perturbation and the flame diameter. The mean velocity and the flame length represents the axial flow and the mass diffusivity and flame diameter shows the radial flow. So, the flame cutting conditions of these experimental conditions is expressed as equation with the Peclet number, flame length, flame diameter, velocity perturbation and correlation coefficient between the velocity perturbation and flame diameter shown as Eqn. (3.1). The numerator of Eqn. (3.1) consists of the axial flow parameter and the numerator of this equation consists of the radial flow parameter.

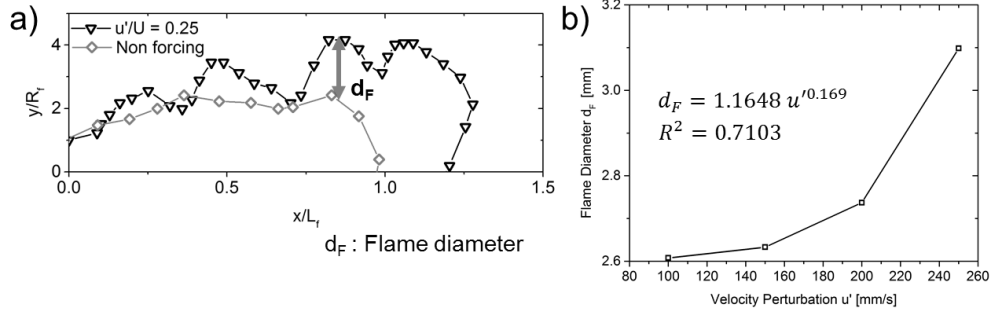


Fig. 3.5 (a) Flame diameter definition with  $U = 1.0$  m/s,  $u' = 0.25$  m/s and  $H_2/CH_4 = 75\%/25\%$ , (b) relation between the flame diameter and the velocity perturbation

$$\frac{U \times d_f}{D} \frac{L_f}{d_F} \left( \frac{1}{u'} \right)^{0.169} f < 0.046 \quad (3.1)$$

The flow oscillation is reflected in the flame surface with 200 and 300 Hz of forcing. In this condition, no flame stagnation or cutting phenomenon occurs. The flame surface consists of continuous undulations of flame. The flame forced by a 200 Hz oscillation consists of seven undulations, while the flame with a 300 Hz forcing consists of 12 undulations. As the forcing frequency increases, the number of undulations and the flame length increase, but the magnitude of undulations decreases. Therefore, the flame area decreases as the forcing frequency is increased from 200 Hz to 300 Hz.

Contrary to these results, the fluctuation of the flame surface with 250 Hz of forcing almost disappears and the flame area reaches its largest value in the range from 100 Hz to 300 Hz. The flame surface and length are affected by the mixing degree, so one reason for this result might be a reduction in the degree of mixing at 250 Hz of forcing compared to the other frequencies. This phenomenon is also seen in the other fuel concentration condition of 50% hydrogen and 50% methane.

### 3.2.2. Velocity dependence on the dynamics of the flame surface

The instantaneous flame surface changes in response to input velocity are shown in Fig.

3.6. The velocity dependence of the flame surface is described by the Peclet number, which consists of the mass diffusivity, the input mean velocity (which is the average velocity during one period), and the fuel nozzle diameter.

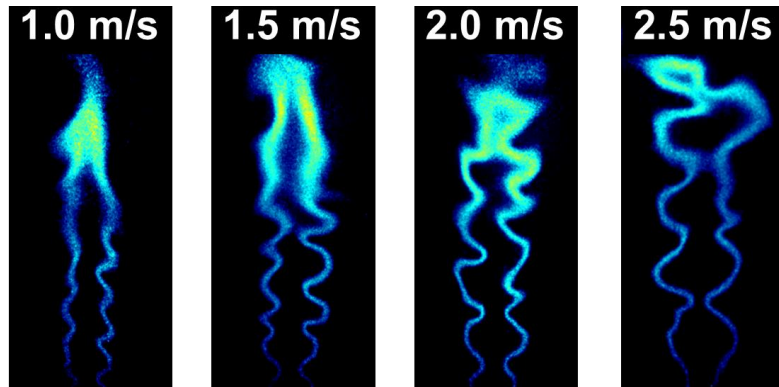


Fig. 3.6 Flame surface with various mean velocities using  $H_2/CH_4 = 75\%/25\%$  and forcing frequency = 300 Hz, determined by OH-PLIF

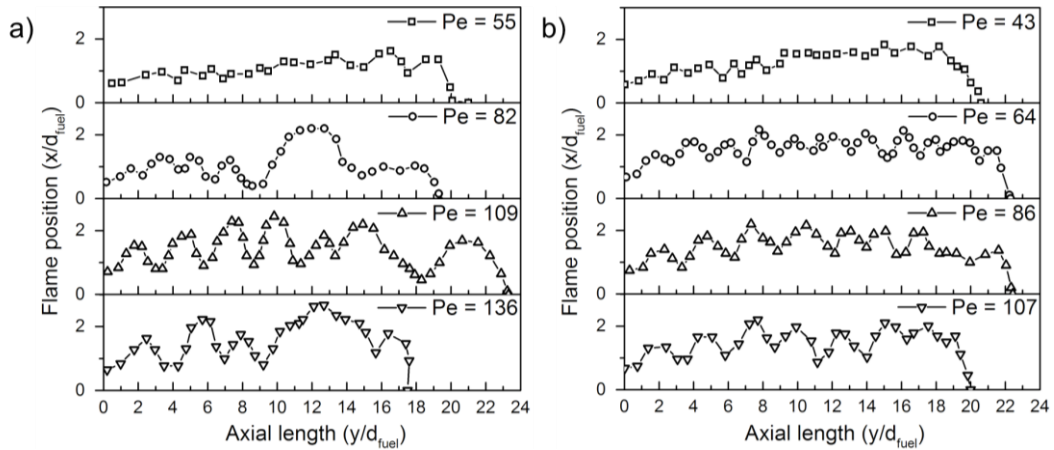


Fig. 3.7 Peclet number's (Pe) dependence of the flame surface using  $u_0 = 1$  m/s at two different fuel concentration condition, (a)  $H_2/CH_4 = 50\%/50\%$ , (b)  $H_2/CH_4 = 75\%/25\%$

Figure 3.7 shows the Peclet number's dependence of the flame surface in the specific condition written indicated in the figure caption. The flame length remains almost constant

as the Peclet number increases. The magnitude of undulations that consists of the flame surface increases with an increasing Peclet number, as shown in Fig. 3.7, but the wavelength of these undulations is nearly the same in all conditions.

The relation between the experimental and analytical values varies depending on the changing parameters. The Strouhal number's dependence varies slightly between the experimental results and the analytical solution, as shown in the 14th reference. The main difference occurs in the flame length, which becomes shorter with acoustic forcing. The flame length changes according to the forcing frequency, but the analytical solution does not reveal this phenomenon. The wavelength of the flame surface oscillations also varies depending on the forcing frequency, decreasing with an increasing forcing frequency.

In contrast, the Peclet number's dependence in the experiments is similar to that found in the analytical solution. The magnitude of flame surface undulations is proportional to the Peclet number, and this relation can also be found in the analytical solution in the 10th reference, which shows that the magnitude of the flame oscillations decreases as the Peclet number increases from 20 to 100, but the flame length barely changes in response to the forcing frequency.

The Strouhal number's dependence on the flame length and surface is larger than that of the Peclet number. Otherwise, the magnitude of oscillations of the flame surface is more sensitive to the Peclet number's change. Therefore, the experimental results indicate that the flame length is significantly affected by the forcing frequency and less affected by the input velocity.

### 3.2.3. Dynamics of heat release

Figures 3.8 and 3.9 show the flame response of acoustic forcing. This study uses the flame transfer function based on chemiluminescence for the analysis of the flame response. The flame surface is not used to measure the heat release rate. The gain of the flame transfer function shows the magnitude of the response depicted in the graph shown in Fig. 3.8. The gain shows that the flame acts as a low-pass filter because the response of the flame to low-frequency forcing is larger than at any other condition. All the flame types have a valley

point on the graph. The forcing frequency causing the valley condition is the same in the non-oscillating condition of the flame surface, as shown in Fig. 3.2. The gain increases as the forcing frequency rises after the valley condition because the magnitude of flame surface undulations reappears after that point. A comparison of Fig. 3.2 and Fig. 3.8 reveals that the gain of the flame transfer function is closely related to the magnitude of undulations on the flame surface.

Both the response of the diffusion flame are inversely proportional to the Strouhal number. The analytical results for the reference are indicated in Fig. 3.8 to compare the experiments with the analytical solution. The dotted line in Fig. 3.8 is the analytical solution of the study published by N. Magina et al. [15]. The main assumptions of Magina et al.'s study involving the Burke-Schumann flame are the following. This flame neglects transverse convection and streamwise diffusion. The main assumption of Schuller et al.'s study involving the premixed flame is that the forcing frequency is low frequency. In this paper, the test condition is controlled to match the assumption of the Burke-Schumann flame. The Peclet number in this study is similar to the value used in the analytical study. In addition, the forcing frequency is relatively low to match the assumption of the premixed flame.

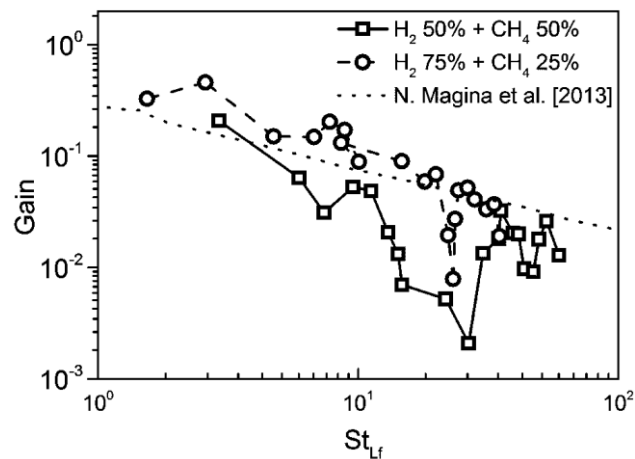


Fig. 3.8 Gain of the flame transfer function of diffusion flame at 1.0 m/s

For the diffusion flame, the gain of the higher hydrogen flame is similar to that of the analytical solution, whereas a slight gap exists in the gain of the lower hydrogen flame between the experiments and analytics because the flame with 50% hydrogen has a wide range of valley conditions. The gain of the 50%/50% flame is scattered. These results are related to the flame length, as shown in Figure 3.3. In the analytical study, the flame length with input flow oscillations is constant in all forcing frequencies, but the flame length changes according to the forcing frequency. The decreasing range of the flame length with forcing coincides with different ranges of gain between the experimental and analytical results. When the experimental flame length is similar to the analytical data, the experimental gain is similar to the analytical results.

The analytical calculation of gain is well matched with the experimental results, except for the valley conditions. Therefore, the analytical calculation of the gain of the flame transfer function can predict the response of the flame.

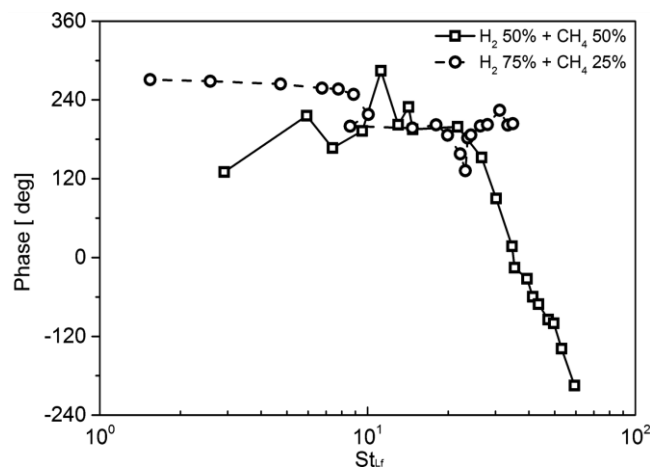


Fig. 3.9 Phase of the flame transfer function of diffusion flames at 1.0 m/s

Figure 3.9 shows the phase of the flame transfer function. This phase shows the potential for combustion instability based on the analysis of the coupling of the flow oscillation and the heat release oscillation.

The phase of the 50%/50% flame is inversely proportional to the Strouhal number when the Strouhal number is higher than 10. Thus, the phase of the 50%/50% flame shows periodical change tendency of degree according to the Strouhal number. The phase of 75%/25% flame decreases as descending the stars when the Strouhal number is near 10. The phase of the flame transfer function shows the possibility of instability. The stability of the 50%/50% flame is sensitive to the forcing frequency because the phase is sensitive to the forcing frequency. In contrast, the 75%/25% flame is relatively stable because the phase does not significantly change.

The phase of the experimental results is not compared with the analytical results. In the non-premixed flame, the measurement point of velocity perturbation is not the same as the location of the flame that emits heat. Therefore, the phase difference occurs not only because of the time delay, but also the position of measurement. In the premixed flame, the experimental phase difference is not well-matched with the analytical results, according to the 3rd reference in this paper. Therefore, the phase is not compared with the analytical results because of the additional phase difference.

### **3.3 Relation between Heat Release and Flame Area**

In this study, the process in which the flame area oscillation transfers to the heat release perturbation as shown in Fig. 1.1(b) is confirmed. The area of the flame is calculated through the flame shape measured by the high speed camera. The flame applied in this study was the form of jet diffusion flame formed at the position where fuel and air are mixed. It is assumed that the thickness of the flame was very thin and the central axis is the rotation axis. The flame surface area was calculated by simulating the three dimensional flame for each flame photograph. The perturbation magnitude of the flame area was calculated by the Fast Fourier Transform. The perturbation value of the calculated flame area which is obtained by dividing by the average flame area was expressed as a function of the frequency.

In this study, flame images were taken to confirm the change of flame shape when the

velocity perturbation occurred at 7000 flames per second. To understand the flickering tendency of flame surface, the instantaneous flame shape was listed as shown in Fig. 3.10. The phenomenon that the flame is cut off was found from 40 Hz to 120 Hz excitation. In this region, the flame is cut off from the second valley of the wave constituting the flame attached to the nozzle

The flame did not break but it consisted of several waves from 140 Hz to 200 Hz. At this time, the amplitude of the wave constituting the flame is reduced as the excitation frequency increases. In the region where the excitation frequency was from 220 Hz to 280 Hz, the flame surface was kept constant without fluctuating in spite of the presence of the fluctuation of the flow. After that, the flame surface began to shake again from 300 Hz, and the degree of tremor decreased with increasing excitation frequency after 320 Hz that made the highest vibration of the flame.

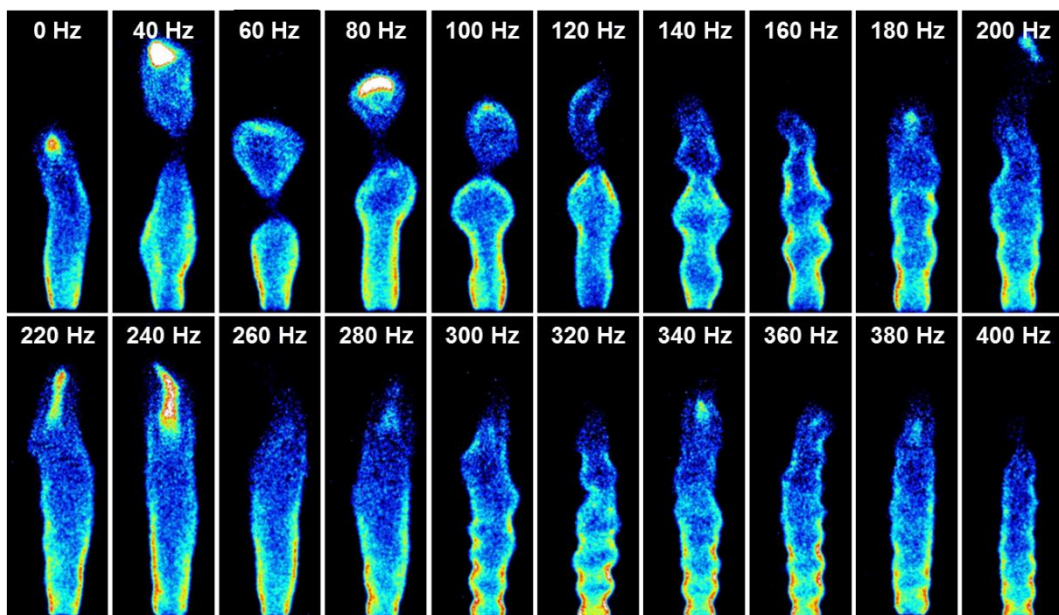


Fig. 3.10 Instantaneous flame surface with various forcing frequencies



The shape of the flames varied greatly according to the excitation frequency in spite of the same velocity perturbation. In addition, the phenomenon that the flame surface was cut off or not almost shaken appeared at the specific frequency. As the frequency increases, the number of waves constituting the flame increases and the amplitude decreases, except for the range where the flame is cut off or not shaken.

In order to investigate the relationship between flame area fluctuation and heat release perturbation, the perturbation value of the flame area was obtained and compared with the gain of the flame transfer function. The perturbation value of the flame area was divided into three variables. First, the total area of the flame was represented. Secondly, it is divided into the cut area of the flame which is broken and the main area of the flame attached to the nozzle in the condition that the flame is broken. These three flame zones were compared with the gain of the flame transfer function as shown in Fig. 3.11.

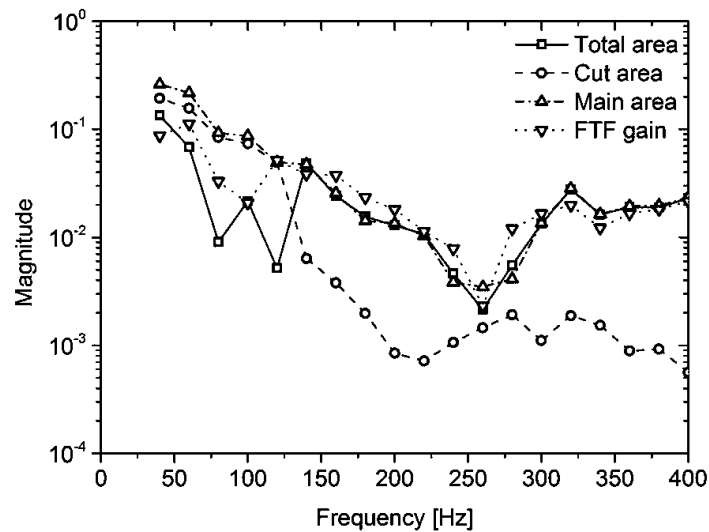


Fig. 3.11 Partial flame area oscillations and gain of flame transfer function

The total flame area perturbation and the attached flame area perturbation were the same at 140 Hz and above because the flame was not cut off, and the gain of the flame transfer function shows a similar value and change tendency to the magnitude of the flame

area perturbation. However, the flame transfer function and the flame area perturbation were not related at all from 40 Hz to 120 Hz where the flame is cut off.

As the frequency increases from 140 Hz to 200 Hz, the degree of the flame area fluctuation decreased. In this region, the gain of the flame transfer function was reduced as much as the degree of the flame area fluctuation decreased. The gain of the flame transfer function was also very low from 220 Hz to 280 Hz where the flame surface is almost not shaken. The minimum gain appeared at 260 Hz, which is the lowest perturbation level. The flame transfer function started to increase again from 300 Hz when the flame surface oscillated, and the gain also became maximum at 320 Hz where the flame oscillated the most in 300 Hz or more. It can be seen that the degree of fluctuation of the flame area is closely related to the fluctuation amount of the heat release expressed by the gain of the flame transfer function except for the low frequency region where the flame is broken.

In the low frequency range where the flame was cut off, not only the flame area fluctuation and the flame transfer function response value were much different, but also the total flame perturbation was much smaller than the area perturbation of the attached flame or the broken flame. In order to confirm this phenomenon, the area change of whole flame, attached flame, and broken flame over time was observed at the flame cut off frequency.

Figure 3.12 showed the change in each flame area when an 80 Hz excitation with flame breaking. The change in the total flame area shown by the solid line did not show the periodicity although the area of the flame varied with time. The reason can be confirmed by the change in the area of the attached flame and the broken flame. The attached flame and the broken flame showed periodicity with time, but the change in flame area showed a phase difference of exactly 180 degrees. Therefore, when the change in the total flame area was measured, the change in the area of the flame was canceled because the area change of the attached flame and the broken flame canceled each other, so that the flame area disappeared. The relationship between the gain of the flame transfer function and the change in the area of the total flame disappeared as the area of the broken flame and the attached flame showed the opposite tendency of change.

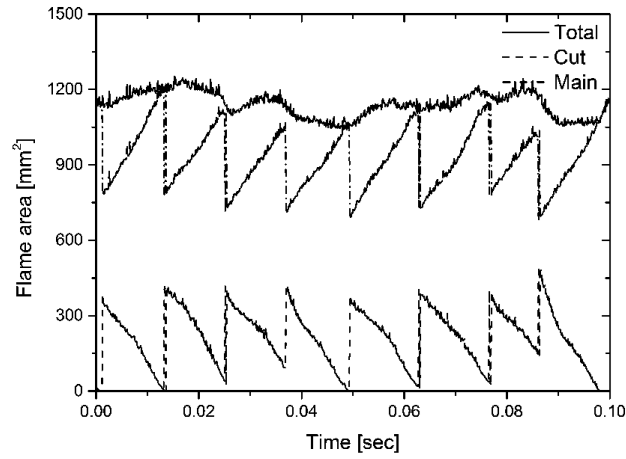


Fig. 3.12 Total and partial flame surface area with 80 Hz forcing frequency

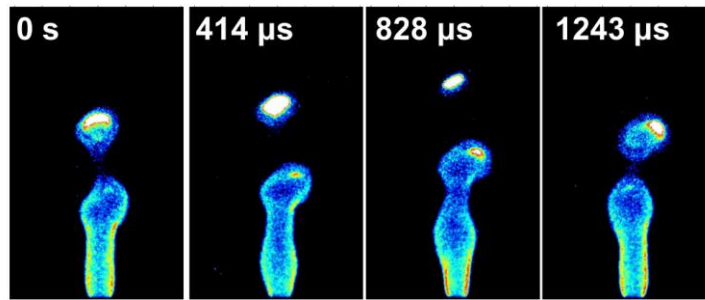


Fig. 3.13 Sequence of flame cutting with 80 Hz forcing frequency

In order to confirm this phenomenon, we measured the moment when the flame was broken with a high speed camera as shown in Fig. 3.13. At the moment when the flame is cut, the flame attached to the nozzle formed a circular broken flame attached to the end of the flame. As soon as the flame is cut, the area of the attached flame decreased sharply and the area of the newly generated broken flame increased. Therefore, the broken flame and the attached flame were formed with a phase difference of 180 degrees as shown in Fig. 3.12.

The figure 3.14 showed the relation between the gain of the flame transfer function and the area perturbation with various experimental conditions. Contrary to fig. 3.11 and 3.12,

the magnitude of the velocity perturbation was constant. Similar to conditions of the flame transfer function, the velocity perturbation was varied in the fig. 3.11 and 3.12. The conditions of the fig. 3.14 was similar to the flame describing function.

The change tendency of the the area perturbation and the gain of the flame transfer function were similar only when the mean velocity was low and the ratio of the hydrogen in fuel was high.

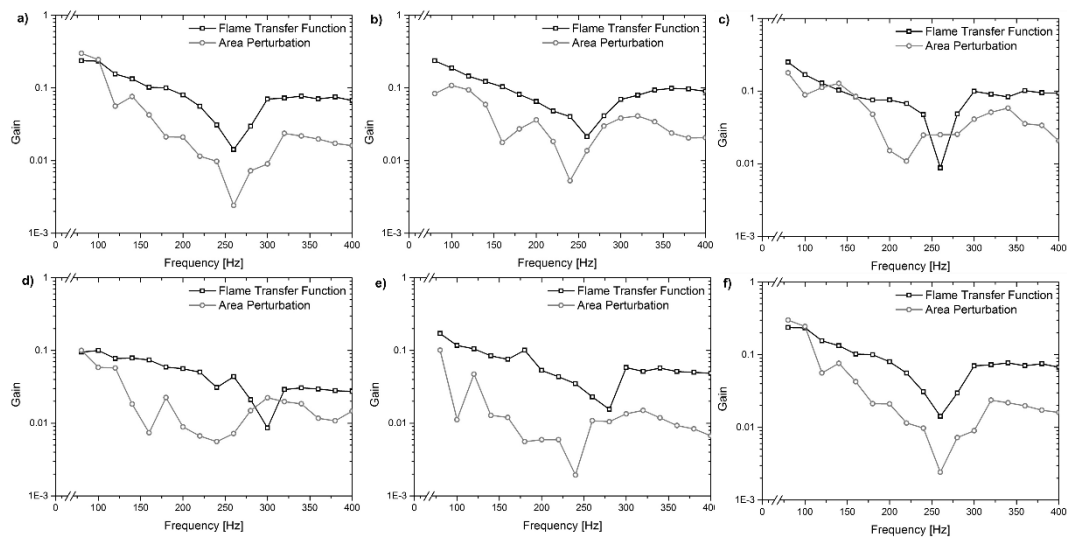


Fig. 3.14 Flame area perturbation and gain of the flame transfer function with (a)  $U = 1.0$  m/s,  $H_2/CH_4 = 75\%/25\%$  and  $u'/U = 0.1$ , (b)  $U = 1.5$  m/s,  $H_2/CH_4 = 75\%/25\%$  and  $u'/U = 0.1$ , (c)  $U = 2.0$  m/s,  $H_2/CH_4 = 75\%/25\%$  and  $u'/U = 0.1$ , (d)  $U = 1.0$  m/s,  $H_2/CH_4 = 25\%/75\%$  and  $u'/U = 0.1$ , (e)  $U = 1.0$  m/s,  $H_2/CH_4 = 50\%/50\%$  and  $u'/U = 0.1$  and (f)  $U = 1.0$  m/s,  $H_2/CH_4 = 75\%/25\%$  and  $u'/U = 0.1$

The figure 3.15 showed the relation between the gain of the flame transfer function and the area perturbation with various magnitude of the velocity perturbation. The lower the speed, the more similar between these two change tendencies. Therefore, the relation between the flame area and heat release are formed in the laminar flow region or low flow

fluctuation.

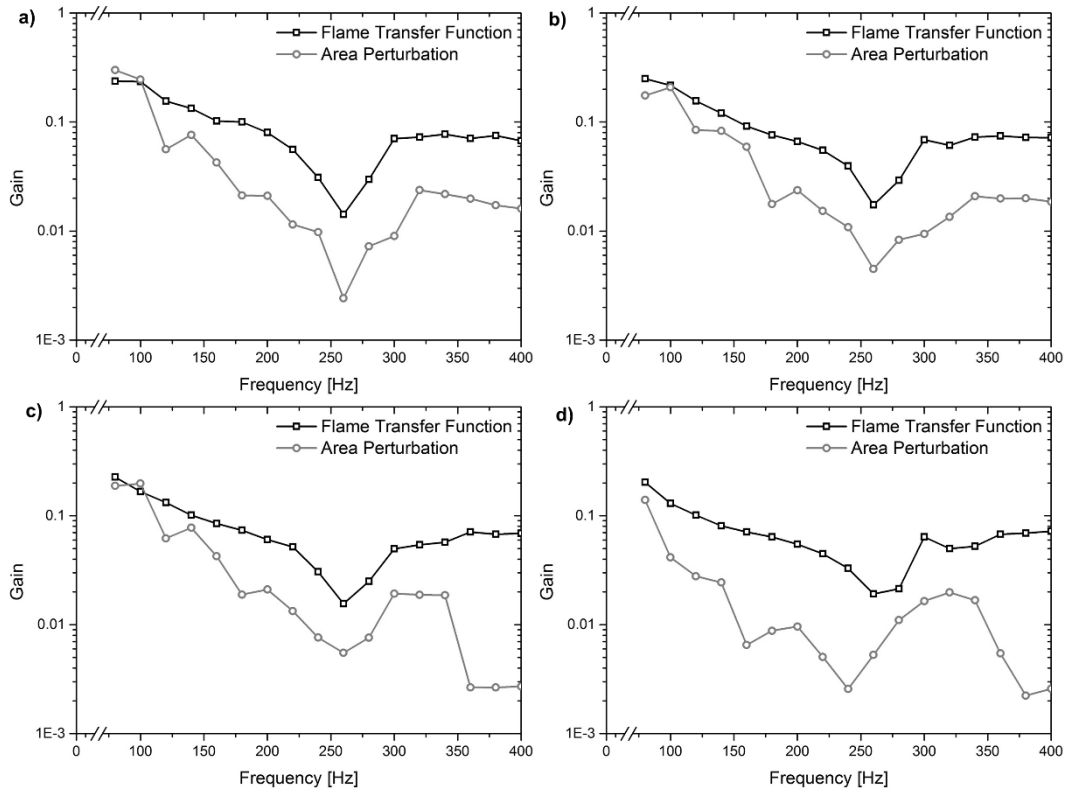


Fig. 3.15 Flame area perturbation and gain of the flame transfer function with  $U = 1.0$  m/s,  $H_2/CH_4 = 75\%/25\%$  and (a)  $u'/U = 0.1$ , (b)  $u'/U = 0.15$ , (c)  $u'/U = 0.2$  and (d)  $u'/U = 0.25$

### 3.4 Effect of Velocity and Mass Diffusivity

#### 3.4.1. Effect on the flame transfer function

The flame transfer function, which shows the relationship between the heat release perturbation and velocity perturbation, is divided into a gain and phase. In addition, to understand the effect of the frequency and flame length, we divided it into the frequency effect and Strouhal number effect. The gain presented in Fig. 3.16(a) has a similar tendency

to change, even if the input mean velocity increases. The lowest point appears at 260 Hz, and the reversal of the value is shown based on this result. In the region of less than 260 Hz, the response value is larger when the velocity is low; however, the response value is higher when the velocity is high for the frequency of 260 Hz or more. From that point, it is confirmed that the value is constant at a certain frequency or higher. For 1.0 m/s, the value does not change significantly after 300 Hz, and it is constant after 340 Hz for 1.5 m/s and 360 Hz for 2.0 m/s. It is confirmed that the increase of the average input velocity affects the saturation condition.

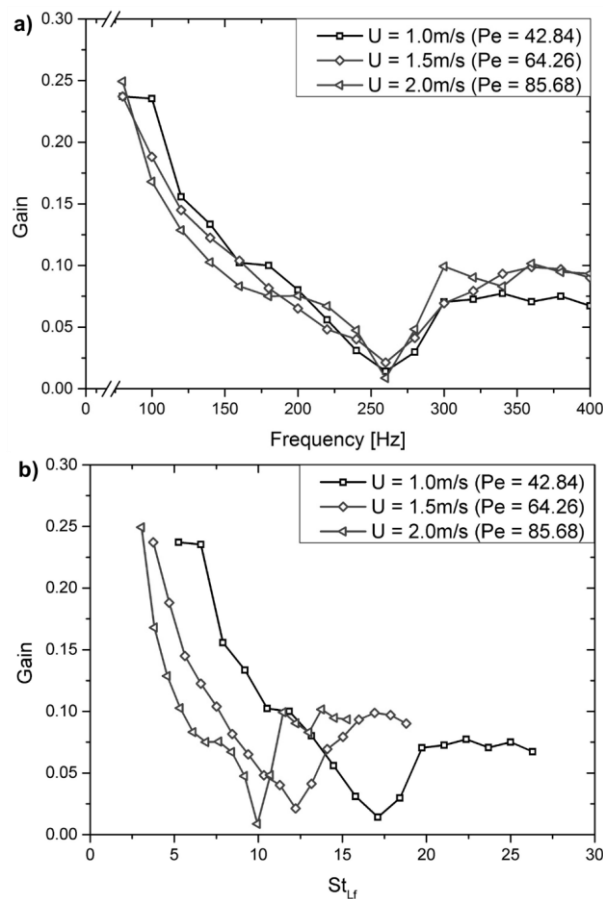


Fig. 3.16 The flame transfer function with various input mean velocities, (a) gain according to forcing frequency, (b) gain according to Strouhal number

The gain of the flame transfer function according to the Strouhal number considering the flame length is shown in Fig. 3.16(b). This graph shows a parallel movement of Fig. 3.16(a) in the x-axis direction due to the increase of the flame length for the velocity increase. When the Péclet number is high, the gain changes more sharply and shows the lowest point at a lower Strouhal number. In other words, it is confirmed that it is more sensitive to the change of the Strouhal number in a high Péclet number.

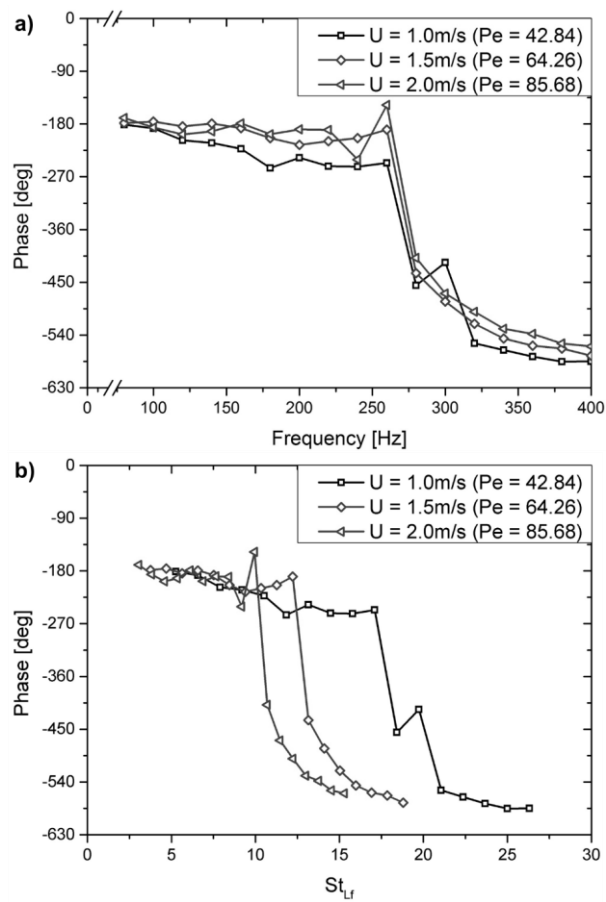


Fig. 3.17 The flame transfer function with various input mean velocities, (a) phase according to forcing frequency, and (b) phase according to Strouhal number

The effect of frequency on the phase shown in Fig. 3.17(a) and (b) depicted a similar tendency of change to that of the gain in all three conditions. The instantaneous phase over 260 Hz, which showed the lowest point of the gain, seemed to drop sharply. As the average velocity increased, the phase difference between the heat release and velocity perturbation decreased. Furthermore, the relationship between the average velocity and phase difference remained constant, unlike the tendency of the gain change. The higher the average velocity was, the more rapid was the increase in the phase difference at the lower Strouhal number. It was thus confirmed that the phase difference is irrelevant to the Péclet number until the rapid change occurs.

The response of the heat release greatly varied in terms of the variation of the fuel composition compared to the average velocity change. The flame response shown in Fig. 3.18(a) exhibits a lower value as the methane ratio increases, and the excitation frequency at which the lowest point appears increases. However, the shape of the graph maintains a constant shape that retains a constant value after increasing slightly after the lowest point, regardless of the fuel composition. The variation of the flame response according to the Strouhal number shown in Fig. 3.18(b) shows that the lowest point is found at the higher Strouhal number when the methane ratio is high. This change tendency is similar to the change in frequency. Additionally, the flame response changes suddenly when the Péclet number is low because the methane ratio is low. In other words, it was confirmed that the response of the heat release according to the Strouhal number is more sensitive to the change of the Strouhal number at the lower Péclet number with a lower methane composition.



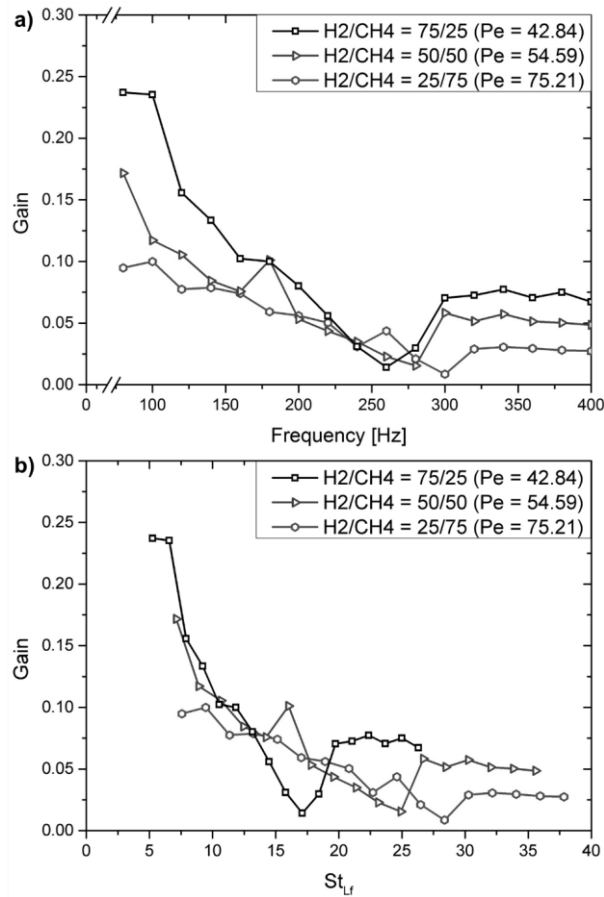


Fig. 3.18 The flame transfer function with various fuel concentrations, (a) gain according to forcing frequency, (b) gain according to Strouhal number

The phase difference according to the frequency shown in Fig. 3.19(a) is slightly larger until a sudden change when the methane ratio is low and drops sharply at a higher frequency with the higher methane ratio. Similar to the gain, a phase difference is almost constantly maintained above 320 Hz without any effect of the frequency change. When the phase difference is described with the Strouhal number in Fig. 3.19(b), the effect of the Péclet number on the phase difference is clearer than the phase with the frequency. At the high methane ratio, a rapid phase difference change occurs at a high Strouhal number, and a markedly large phase difference is observed at a low methane ratio.

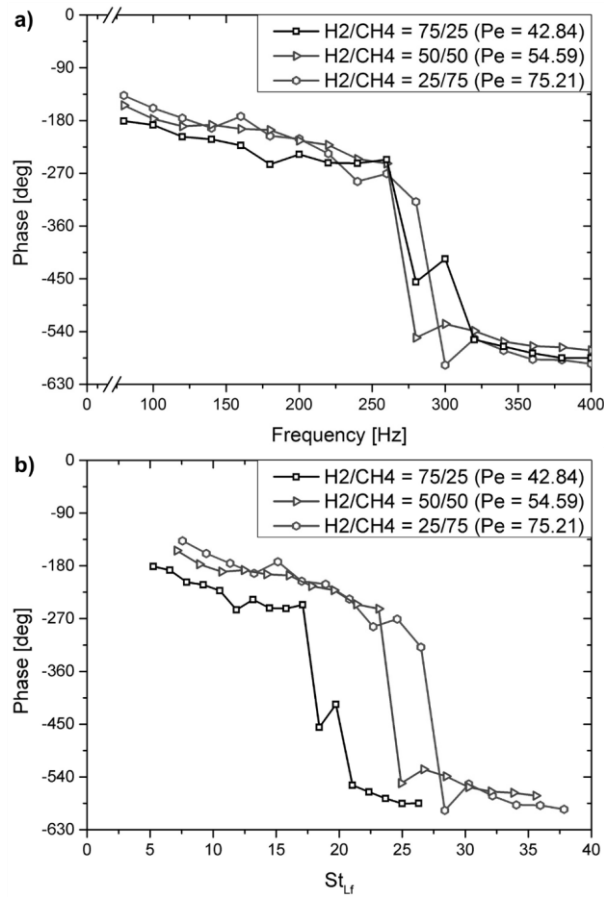


Fig. 3.19 The flame transfer function with various fuel concentrations, (a) phase according to forcing frequency, and (b) phase according to Strouhal number

### 3.4.2. Effect on the flame shape

Fig. 3.20 shows the change of real flame shape of the same velocity phase with an increasing mean velocity and the methane ratio of the fuel. Fig. 3.21 shows the schematic flame shape based on the Fig. 3.20.

Fig. 3.21(a) shows the change of flame shape with an increasing input mean velocity. The flame shape is represented by the instantaneous shape of the same phase of velocity when the flow was forced at 100 Hz. This forcing frequency makes an obvious curved flame surface. The flame surface in the figure is dimensionless in the axial direction with

the flame length of the steady state, and in the transverse direction with the diameter of the fuel nozzle. The flame consists of several waves. When the input velocity is 1.5 m/s, the flame is composed of three waves with a 100 Hz excitation, considering a slight distortion in the middle of the last wave. As the velocity increases, the amplitude of the waves constituting the flame increases, and the ratio of the first wave to the entire flame increases.

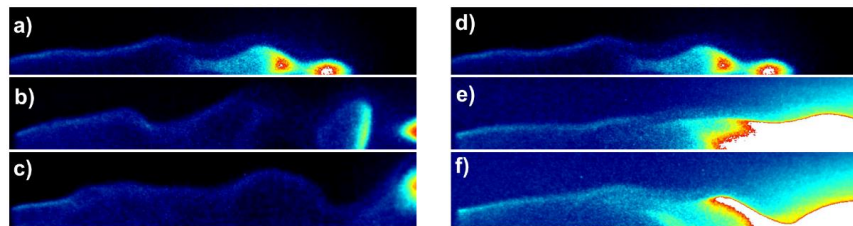


Fig. 3.20 Instantaneous real flame shape at (a)  $U = 1.0$  m/s, (b)  $U = 1.5$  m/s, (c)  $U = 2.0$  m/s with  $H_2/CH_4 = 75/25$ ,  $f = 100$  Hz and (d)  $H_2/CH_4 = 75/25$ , (e)  $H_2/CH_4 = 50/50$ , (f)  $H_2/CH_4 = 25/75$  with  $U = 1.0$  m/s,  $f = 100$  Hz

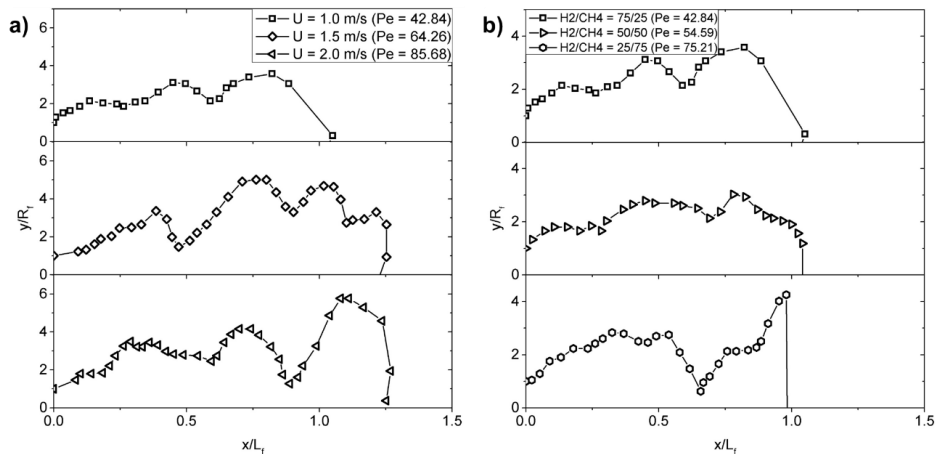


Fig. 3.21 Instantaneous schematic of flame shape at (a) three different input mean velocities with  $H_2/CH_4 = 75/25$ ,  $f = 100$  Hz and (b) three different fuel concentrations with  $U = 1.0$  m/s,  $f = 100$  Hz

Fig. 3.21(b) shows the flame shape according to the changing fuel composition. As the methane ratio in the fuel increases, incomplete combustion occurs and the flame length increases sharply. When the methane ratio of the fuel is 50% or 75%, incomplete combustion occurs and the flame length increases on account of soot. When the ratio of methane is 50%, the length of the flame is 89 mm without excitation. However, the flame is formed outside the field of view of 95 mm maximum with excitation in this fuel concentration. It can be predicted that the mixedness of fuel and air is decreased with the increase of soot generation with excitation. Fig. 3.21(b) shows that, except for 75% of methane, in which the flame generally deviates from the field of view, the flame shape of the other two cases demonstrate that the number of waves constituting the flame remains constant, similar to Fig. 3.21(a). Except for soot generation, the shape of the flame of methane 25% and methane 50% is not significantly different.

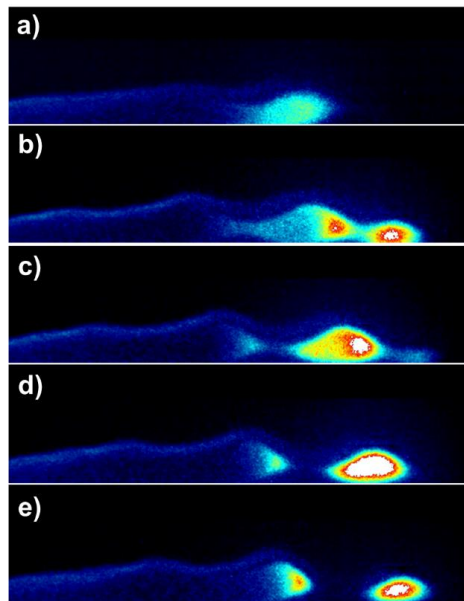


Fig. 3.22 Instantaneous real flame shape at steady state and forced state with one period every 90 degrees with  $H_2/CH_4 = 75/25$ ,  $U = 1.0$  m/s,  $u/U = 0.1$ ,  $f = 100$  Hz

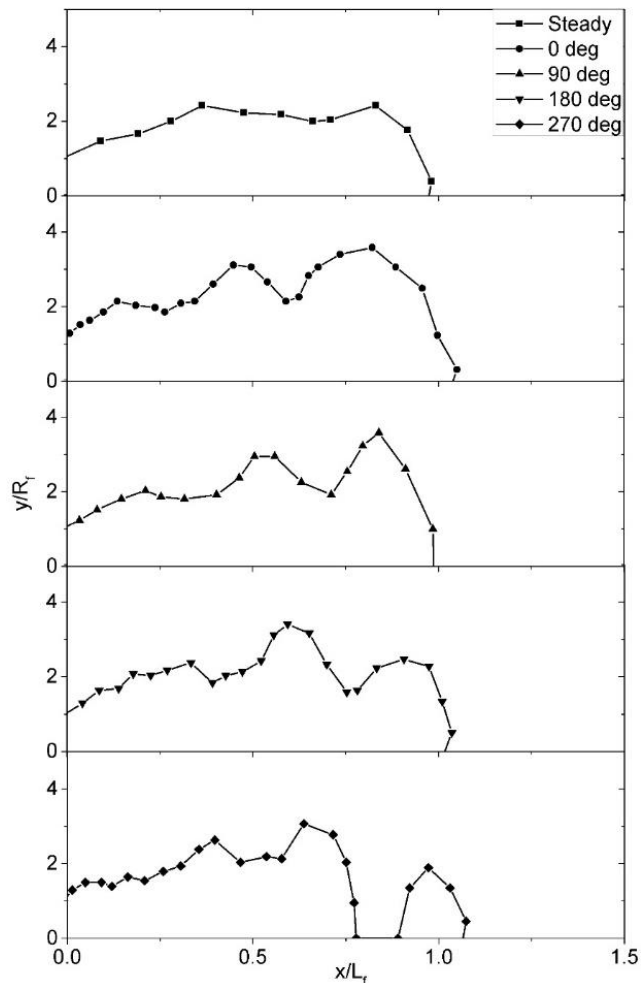


Fig. 3.23 Instantaneous schematic diagram of the flame shape at steady state and forced state with one period every 90 degrees with  $H_2/CH_4 = 75/25$ ,  $U = 1.0$  m/s,  $u/U = 0.1$ ,  $f = 100$  Hz

Flames in all three conditions were longer than those without excitation, and the rate of lengthening showed a slight increase with the increasing velocity. It is generally known that flame length is decreased when fuel or air is forced on one side [37]. To identify flame length changes with the excitation, the flame shapes were compared in cases with and without excitation, as shown in Fig. 3.22 and Fig. 3.23. The phase degree shown in the

figure was calculated based on the measured velocity at the hot wire. As the phase increases, the three waves that constitute the flame move forward. It is evident in the figure that the final wave breaks when the phase is 270 degrees. Moreover, it can be confirmed that the flame exists at the furthest position at this time. Except for the situation in which the flame is broken, the flame length is not significantly different from the case without the flame. It was confirmed that the velocity perturbation caused by the simultaneous excitation of the air and the fuel does not affect the length of the flame.

## 3.5 Nonlinear Dynamics

### 3.5.1. Flame describing function

Nonlinear phenomena on external perturbations are shown as flame description function and harmonic flame transfer function. The flame describing function shows the response characteristics of the flame to the external disturbance magnitude, and the harmonic flame transfer function shows the effect of the perturbation of the specific frequency on the 2nd harmonic frequency.

In the case of the flame transfer function for velocity perturbation named as the flame describing function, only the influence of the frequency is recognized because the flame length used for the Strouhal number is the same in all cases. The gain in Fig. 3.24(a) shows the lower value when the velocity perturbation is higher until 260 Hz, which shows the lowest value and almost the same value for all cases. Then, the gain is restored and is slightly large when the velocity perturbation is small after 260 Hz. Nevertheless, the same gain is obtained under all conditions at the frequency of 360 Hz or more. The phase difference of Fig. 3.24(b) shows almost the same value except 300 Hz. At 300 Hz, the phase perturbation gradually decreases from 0.1 m/s to 0.2 m/s, and the phase difference does not change from 0.2 m/s. Through the flame transfer function, the velocity perturbation and heat release perturbation are nonlinear in the range of 80 Hz to 400 Hz and 0.1 m/s to 0.2 m/s.

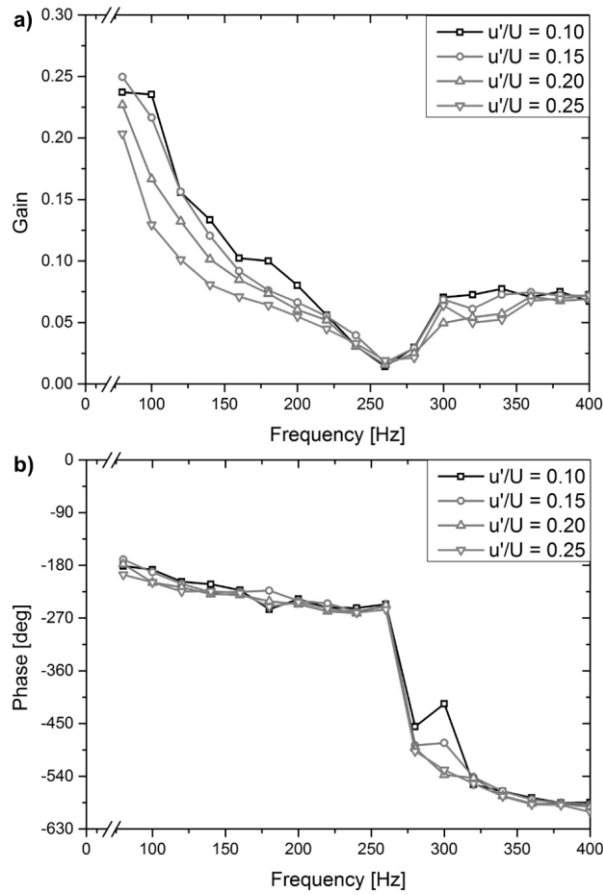


Fig. 3.24 Flame transfer function with various velocity perturbation magnitudes according to forcing frequency, (a) gain, (b) phase

Figure 3.25 and 3.26 depicts a flame shape at the same velocity phase while varying the velocity perturbation from 0.1 m/s to 0.25 m/s. When the velocity perturbation is 0.1 m/s and 0.15 m/s, the flame consists of three waves; however, it consists of four waves at 0.25 m/s. In addition, as the flame consists of four waves, it is confirmed that the flame length also increases. However, the ratio between the flame length and the first wave of the flame is kept constant.

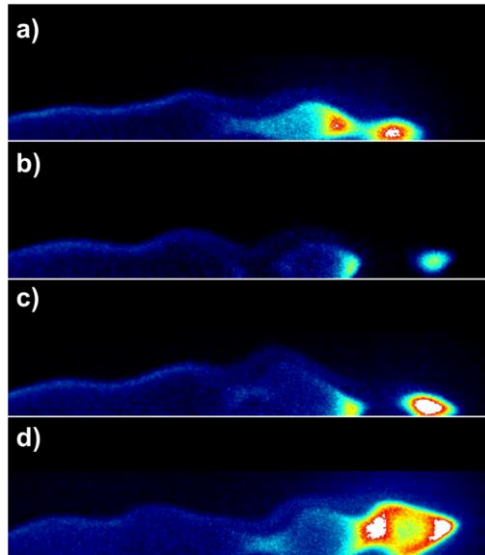


Fig. 3.25 Instantaneous real flame shape at four different velocity perturbations

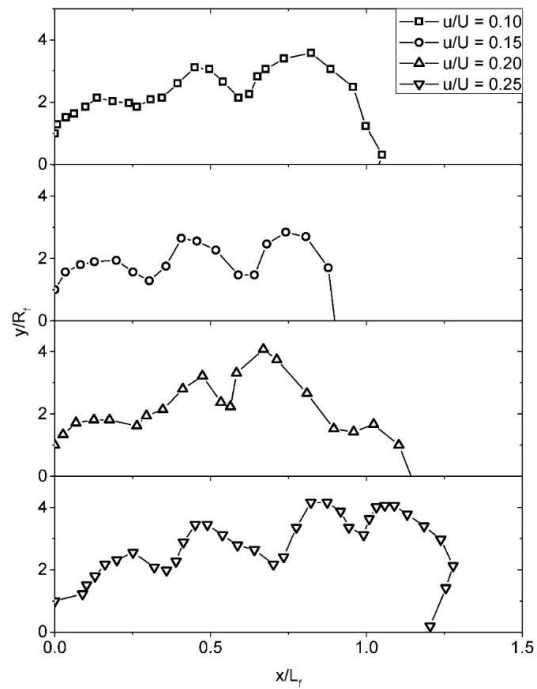


Fig. 3.26 Instantaneous schematic diagram of the flame shape at four different velocity perturbations



### 3.5.2. Harmonic flame transfer function

Figure 3.27 and 3.28 showed the effect of perturbation on 2nd harmonic frequency by fuel composition. The effect on the air velocity perturbation shown in Fig. 3.27(a) showed the greatest value at 260 Hz, which was the same frequency in all compositions. The effect of fuel composition on the second harmonic was the largest at the same composition of hydrogen and methane. The effect on the 2nd harmonic frequency decreases as increasing the hydrogen ratio.

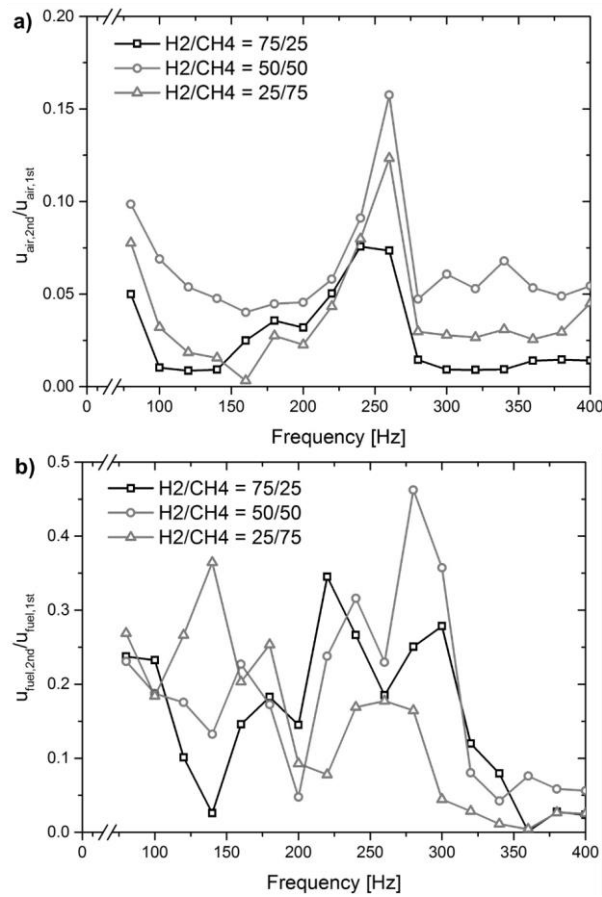


Fig. 3.27 Normalized 2nd harmonic response with various fuel composition according to forcing frequency, (a) air velocity, (b) fuel velocity

In the case of fuel perturbation, three peaks were observed according to the frequency. When the ratio of methane to fuel is high, the effect on 2nd harmonic frequency is large at the low frequency. The absolute magnitude of the second-order magnitude is large when the ratio of methane to hydrogen is the same regardless of air or fuel perturbation, and is lowest when the hydrogen ratio is high.

This tendency is different in the heat release of Fig. 3.28. The effect on the heat release is most significant at high methane rates and lowest at the same methane and hydrogen ratio. The frequency at which the 2nd harmonic is most affected is the same as when the gain is the minimum value in Fig. 3.27(a). This shows that the effect on the 2nd harmonic heat release is greatest at the point where the 1st harmonic heat release is minimized. As one of the reasons for the low 1st heat release, energy transfer to the 2nd harmonic heat release can be deduced.

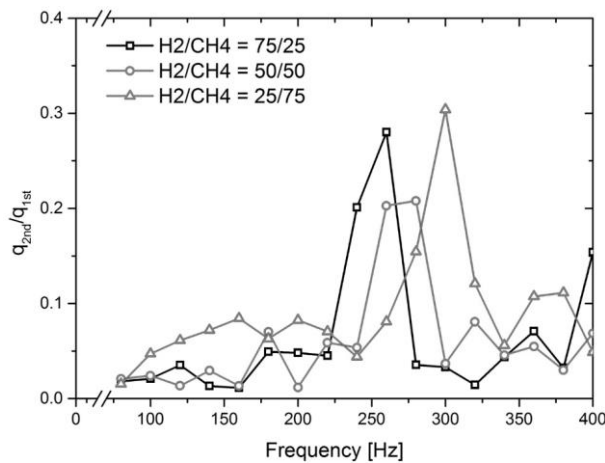


Fig. 3.28 Normalized 2nd harmonic heat release response with various fuel composition according to forcing frequency

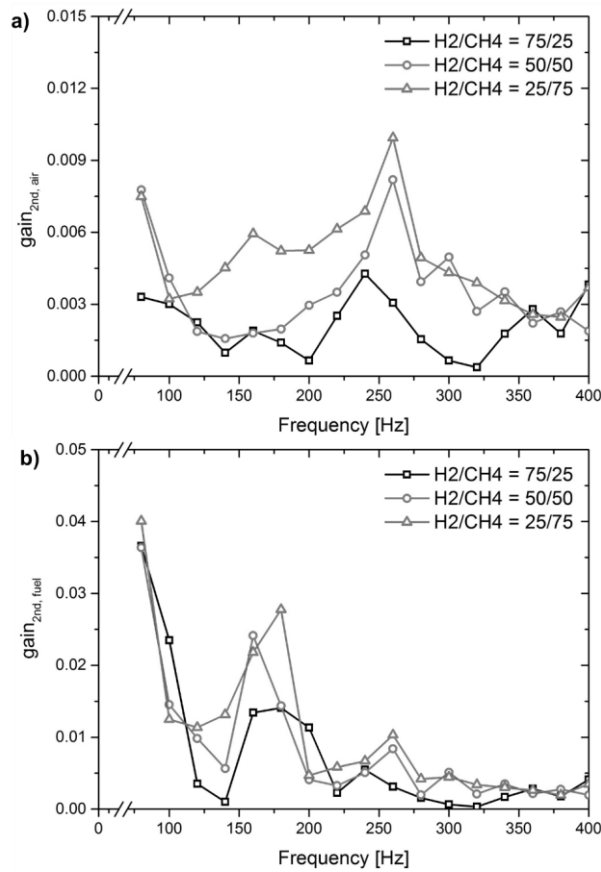


Fig. 3.29 Normalized 2nd harmonic response with various fuel composition according to forcing frequency, (a) gain of the flame transfer function with air velocity, (b) gain of the flame transfer function with fuel velocity

Fig. 3.29(a) shows the gain of 2nd harmonic flame transfer function based on the magnitude of air perturbation. Overall, the magnitude of gain is high when the rate of methane is high and the frequency of peak increases with increasing methane ratio. Also, although the order of magnitude is different, the tendency of change is similar to that of air velocity perturbation. The 2nd harmonic flame transfer function shown in Fig. 3.29(b) acts as the low pass filter and shows a similar tendency to that of the 1st harmonic flame transfer function. The 2nd flame transfer function based on the fuel perturbation shows a peak at

the same condition of peak of the velocity perturbation shown in Fig. 3.27(b), but the magnitude of the gain decreases with increasing frequency regardless of the magnitude of the velocity perturbation.

In the flame transfer function of the two criteria, a large response value is obtained when the methane ratio is the highest, and the response value is decreased with increasing hydrogen. This phenomenon is the directly opposite to the trend of Fig. 3.18(a). As a result, the influence on the 1st harmonic heat release is low when the methane ratio is high, and thus the effect on the 2nd harmonic heat release is large.

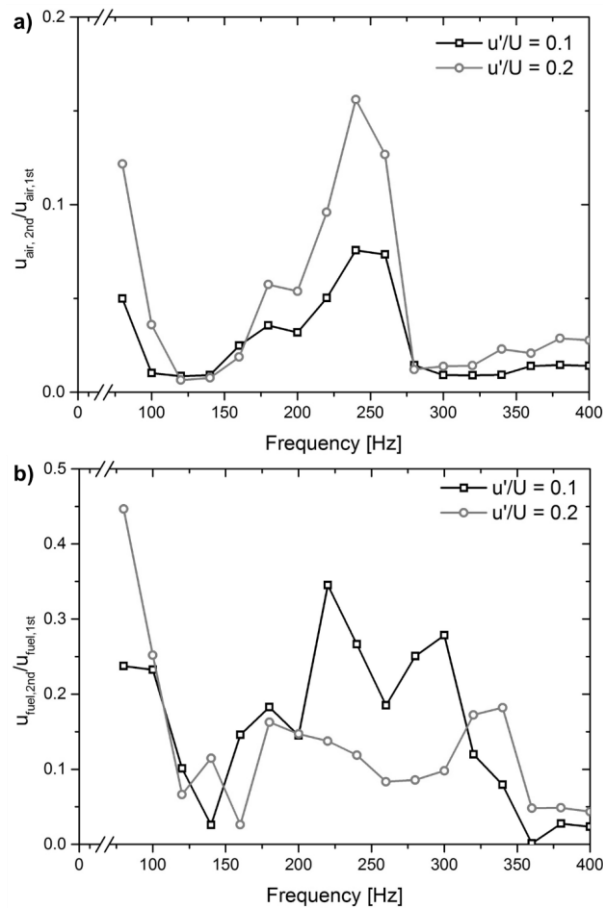


Fig. 3.30 Normalized 2nd harmonic response with various velocity perturbations according to forcing frequency, (a) air velocity, (b) fuel velocity

The effect of the velocity perturbation magnitude and the influence on the 2nd harmonic frequency are shown in Fig.3.30. In the case of the air velocity perturbation shown in Fig. 3.30(a), the effect of the velocity perturbation on the second harmonic frequency is large when the velocity perturbation corresponding to the denominator of the flame transfer function is large, and the tendency to change with frequency is similar. However, in the case of the fuel velocity perturbation of Fig. 3.30(b), the effect on the second harmonic frequency is generally large when the velocity perturbation is low, and the tendency of the change also varies with the perturbation magnitude. Despite the different effects on the velocity perturbation, the rate between 1st harmonic and 2nd harmonic frequency of the heat release shown in Fig. 3.31 is the same regardless of the velocity perturbation. The frequency at which the ratio of the heat release rate is maximum is the condition which makes the first harmonic flame transfer function as minimum value shown in Fig. 3.24.

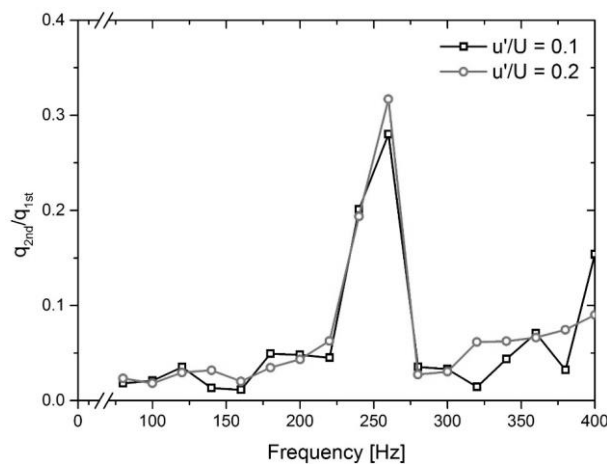


Fig. 3.31 Normalized 2nd harmonic heat release response with various velocity perturbations magnitudes according to forcing frequency

The 2nd harmonic flame transfer function is calculated by this velocity perturbation and heat release perturbations in Fig. 3.32(a) and (b). Because the velocity perturbations of

air and fuel are different, the response of the flame transfer function varies, but the magnitude of the 2nd harmonic flame transfer function increases when the magnitude of the 1st harmonic flame transfer function decreases. In addition, the influence of the velocity perturbation magnitude is not significant when only the first harmonic frequency is considered, but the effect of the velocity perturbation magnitude is generally considered when the second harmonic frequency is considered.

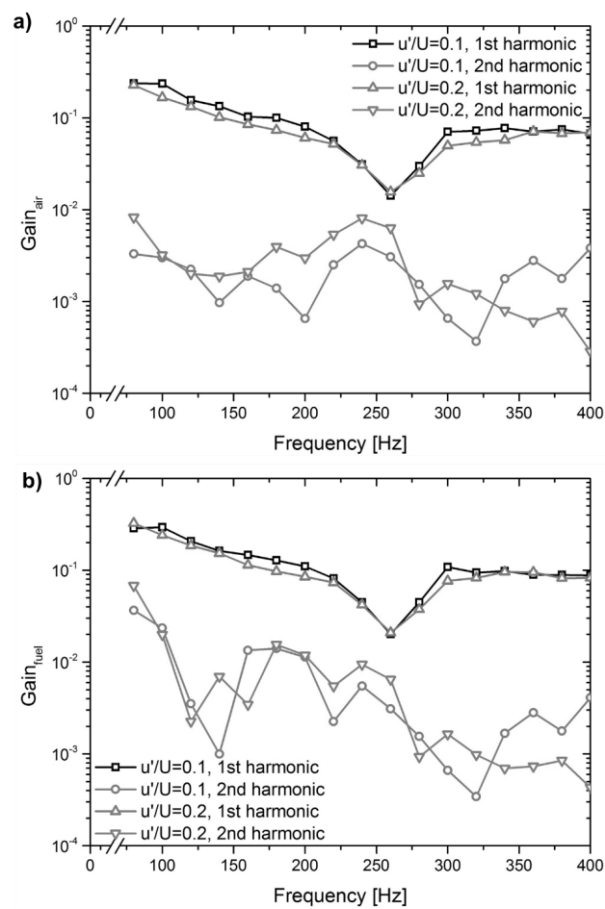


Fig. 3.32 Normalized 2nd harmonic response with various velocity perturbation magnitudes according to forcing frequency, (a) gain of the flame transfer function with air velocity, (b) gain of the flame transfer function with fuel velocity

## **CHAPTER 4**

# **EFFECT OF CLOSED BOUNDARY ON THE DYNAMICS OF THE BURKE-SCHUMANN FLAME**

### **4.1 Objectives and Conditions**

Previous flame dynamic characteristics and combustion instability studies have proceeded in grasping the dynamic characteristics such as flame transfer function except the acoustic effect in the feedback loop generating combustion instability and predicting combustion instability by adding the influence of acoustics to the flame dynamic characteristics. In this process, the influence of the boundary of the combustor, which is the middle stage of the feedback loop for generating the combustion instability, on the flame and the flow had not been much studied. Therefore, this study tried to investigate the effect of the acoustic boundary of the combustor on the flow and heat release.

In this study, we measured the velocity perturbation, heat release perturbation, and pressure perturbation under same conditions except for the presence or absence of the rear end boundary of the combustor. The first purpose of this chapter was to understand the phenomenon that occurs when the acoustic boundary existed in the combustor. In addition, the nonlinear dynamic characteristics of the flame were investigated according to the presence or absence of the acoustic boundary.

The effect of resonant frequency on velocity perturbation was investigated by changing the resonant frequency inside the combustor chamber as the combustor length was varied. The second purpose of this chapter was to investigate the degree of amplification or attenuation by the resonance frequency in the combustor chamber when external disturbance occurred.

Finally, the flame dynamic characteristics at the open boundary and the amplification phenomenon caused by the resonant frequency at the closed boundary were correlated under the condition of combustion instability. The purpose was to investigate the

relationship between the flame dynamic characteristics and the combustion instability.

Velocity perturbations and the hear release perturbations were measured in the same method as in chapter 3. The minimum length of the closed combustor is approximately equal to the length of the flame without excitation as shown in Fig. 3.3. The length was set to 100 mm when  $H_2 / CH_4 = 75\% / 25\%$  and 140 mm when  $H_2 / CH_4 = 50\% / 50\%$ . The maximum length of the closed combustor is set to 620 mm, which is the maximum position of the movable nozzle in Fig.2.2.

Table 4.1 Summary of the test conditions

<b>Parameters</b>	<b>Comparison between open and closed boundary</b>	<b>Effect of combustor length</b>	<b>Relation with combustion instability</b>	<b>unit</b>
<b>Fuel composition</b>	75/25	75/25, 50/50	75/25	$H_2[\%]/CH_4[\%]$
<b>Flow velocity</b>	1.0	1.0	1.0	m/s
<b>Velocity perturbation</b>	0.1, 0.2	0.1, 0.2	-	m/s
<b>Combustor Length</b>	500	100 (140) ~ 620	100 ~ 600	mm
<b>Forcing Frequency</b>	80 ~ 400		-	Hz

In order to confirm the effect of the exhaust duct at the top of the moving nozzle, an orifice having a diameter of 15 mm was mounted at a position of 620 mm in the length of the combustion chamber, which is the maximum moving distance of the nozzle.

The speaker voltage setting for the velocity perturbation occurred at 620 mm, which is the maximum length of the combustor. This speaker voltage setting was fixed when the



combustor length changed. The dynamic pressure was measured at DP 1 as shown in Fig. 2.2 because the dynamic pressure can be measured even under the minimum length of the combustor conditions.

To determine the effect of the acoustic boundary, the length of the closed combustion chamber was set to 500 mm, which is equal to the length of the quartz used in the open end condition. Other experimental conditions are summarized in the table 4.1.

## **4.2 Resonant Frequency of the Combustor**

As the closed boundary is formed in the combustion chamber, the flow inside the combustion chamber was affected by the resonance frequency of the combustion chamber. The resonance frequency is proportional to the speed of sound and is inversely proportional to the length of the combustor. The speed of sound is proportional to the square root of the temperature, so the resonant frequency is proportional to the square root of the temperature and is inversely proportional to the length of the combustor.

The temperature inside the combustion chamber was required to obtain the resonance frequency. Most of the air entering the combustion chamber did not participate in the reaction, and the temperature difference between the central part where the flame was formed and the wall where the air flows was very large. In addition, when the combustor length is 620 mm that is maximum value, there was not enough space for sufficient mixing of the combustion product gas with air considering the flame length of 100 mm. Therefore, in order to obtain the resonant frequency, the error may be increased to apply the adiabatic flame temperature used commonly. In this study, the Burke-Schumann flame was implemented and the temperature was calculated using CHEMKIN PRO that is a chemical species calculation program.

Figure 4.1 showed the temperature obtained by co-flowing non-premixed jet flame by using CRESLAF model of user routines of CHEMKIN PRO experimental conditions of this study. This model is applicable to laminar non-premixed flames, assuming a very thin sheet, although the thickness of the flame side to be burned is present. Most of the regions

maintained the initial air temperature condition and only the region where the flame was formed showed a very high temperature. The adiabatic flame temperature of the experimental conditions obtained by CHEMKIN PRO was 366 K, which is significantly different from the temperature distribution of Fig. 4.1.

The resonance frequency of the combustor was obtained through COMSOL MULTIPHYSICS using the temperature distribution in Fig.4.1. The resonance frequency was calculated by using the length of the combustor from 100 mm to 600 mm at intervals of 50 mm. The temperature used to calculate the resonant frequency was the average of the temperature distribution in Fig. 4.1. The average temperature along the length of the combustor was shown in Table.4.2. Since there was no acoustical boundary between the air and fuel lines and the combustion chamber, the resonance frequency was determined from the bottom of the air line.

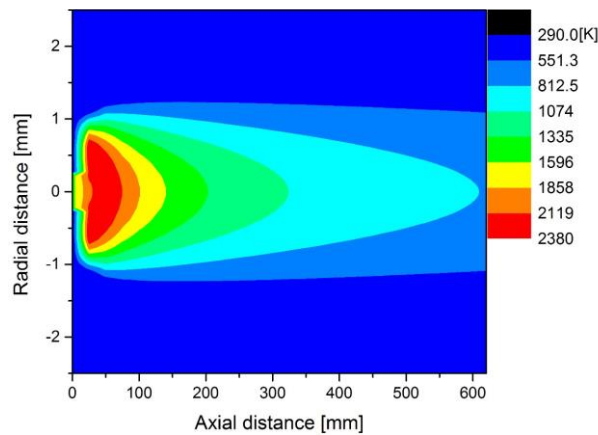


Fig. 4.1 Temperature distribution calculated by CHEMKIN PRO

The resonant frequencies are calculated for four types of structures. First, the calculation from the bottom of the air line to the movable nozzle of Fig.2.2 was shown in Table.4.3. The range of the second calculation shown in Table.4.4 was from the bottom of the air line to the upper part of Fig.2.2 up to 620mm with the movable nozzle. The third shown in Table.4.5 is calculated from the bottom of the air line to the orifice at the top of

the combustion chamber with including a movable nozzle in the middle. Finally, the resonance frequency was calculated considering the exhaust duct corresponding to 1.8m and it was shown in Table.4.6. Considering the exhaust duct, the resonant frequency was calculated using 298 K because there is sufficient space for mixing of the combustion products and air and a sufficient length was secured to approximate the ambient temperature.

Table 4.2 Averaged temperature of the combustor

<b>Combustor length [mm]</b>	<b>100</b>	<b>150</b>	<b>200</b>	<b>250</b>	<b>300</b>	<b>350</b>	<b>400</b>	<b>450</b>	<b>500</b>	<b>550</b>	<b>600</b>
<b>Average temperature [K]</b>	899	844	800	766	738	714	694	677	662	649	637

Table 4.3 Resonant frequency from bottom of air line to movable nozzle

<b>Combustor length [mm]</b>	<b>1st harmonic frequency</b>	<b>2nd harmonic frequency</b>	<b>3rd harmonic frequency</b>
<b>100</b>	131.33	478.45	916.48
<b>150</b>	117.67	432.26	846.17
<b>200</b>	106.88	398.93	791.19
<b>250</b>	98.198	373.44	742.37
<b>300</b>	91.04	352.87	694.77
<b>350</b>	85.027	335.59	646.75
<b>400</b>	79.946	320.66	599.62
<b>450</b>	75.551	307.33	555.7
<b>500</b>	71.355	294.44	516.17
<b>550</b>	68.161	283.55	482.16
<b>600</b>	65.359	272.38	452.94

Table 4.4 Resonant frequency from bottom of air line to end of the combustor

<b>Combustor length [mm]</b>	<b>1st harmonic</b>	<b>2nd harmonic</b>	<b>3rd harmonic</b>
<b>100</b>	205.18	395.86	626.74
<b>150</b>	196.31	390.62	588.02
<b>200</b>	188.68	385.41	569.18
<b>250</b>	182.11	378.5	597.75
<b>300</b>	176.42	369.68	586.29
<b>350</b>	171.46	359.89	607.42
<b>400</b>	167.14	350.07	609.97
<b>450</b>	163.4	340.82	591.73
<b>500</b>	160.2	332.46	566.85
<b>550</b>	157.48	325.14	542.37
<b>600</b>	155.47	319.25	521.71

Table 4.5 Resonant frequency from bottom of air line to end of the combustor with orifice

<b>Combustor length [mm]</b>	<b>1st harmonic</b>	<b>2nd harmonic</b>	<b>3rd harmonic</b>
<b>100</b>	172.76	344.67	571.95
<b>150</b>	166.34	337.57	532.69
<b>200</b>	160.82	333.55	502.59
<b>250</b>	156	331.43	482.8
<b>300</b>	151.71	329.81	473.43
<b>350</b>	147.88	327.52	474.81
<b>400</b>	144.41	323.81	486.08
<b>450</b>	141.26	318.79	502.33
<b>500</b>	138.43	312.97	510.7
<b>550</b>	135.84	306.79	503.47
<b>600</b>	130.89	298.88	485.29

Table 4.6 Resonant frequency from bottom of air line to end of the exhaust duct

<b>Length [mm]</b>	<b>1st</b>	<b>2nd</b>	<b>3rd</b>	<b>4th</b>	<b>5th</b>	<b>6th</b>	<b>7th</b>	<b>8th</b>
<b>100</b>	47.203	110.14	151.93	214.17	255.33	329.17	367.33	431.87
<b>150</b>	47.232	109.46	151.31	216.33	256.18	324.43	362.09	433.9
<b>200</b>	47.259	108.68	150.85	218.18	255.84	320.65	363.2	436.42
<b>250</b>	47.281	107.82	150.55	219.74	254.22	319.87	368.54	439.13
<b>300</b>	47.301	106.95	150.43	220.69	251.91	321.66	377.05	441.13
<b>350</b>	47.317	106.08	150.47	220.84	249.7	324.49	386.45	439.57
<b>400</b>	47.33	105.27	150.66	220.17	248.16	327.32	392.03	434.39
<b>450</b>	47.338	104.51	150.96	218.78	247.43	329.66	389.43	431.31
<b>500</b>	47.343	103.85	151.37	216.94	247.47	331.32	380.58	431.85
<b>550</b>	47.344	103.31	151.88	214.96	248.14	331.91	370.8	433.96
<b>600</b>	47.34	103	152.48	213.19	249.36	330.72	364.15	436.65

Table 4.3 and 4.4 showed the influence of the space behind the nozzle on the resonance frequency. Considering the space behind the nozzle, the changing width of the resonant frequency varying with the length of the combustor was reduced. Also, the harmonic resonant frequency decreased due to the increase in the length of the resonant frequency. The influence of the presence of the orifice on the resonant frequency can be confirmed from Tables 4.4 and 4.5. When the orifice was present at the top of the combustor, the resonance frequency decreased at the same length. Considering the exhaust duct at the top of the combustor, the variation width of the resonance frequency according to the nozzle position was greatly reduced due to the rapid increase in the length considered.

Figure 4.2 and 4.3 simultaneously showed the two resonant frequencies affecting the combustion chamber for the condition that the orifice was mounted on the closed boundary and the closed boundary without orifice. The point where the two resonant frequencies crossed each other will have the greatest effect of the resonant frequency. Figure 4.2

showed the resonance frequency up to the movable nozzle and the resonance frequency up to the exhaust duct, which was estimated by the resonance frequency affecting the combustion chamber of the closed boundary without orifice. The first harmonic frequency of the resonant frequency to the movable nozzle had the intersection of 100 Hz with the 2nd harmonic frequency of the resonant frequency to the exhaust duct at around 200 mm. The 2nd harmonic resonant frequency up to the nozzle had an intersection of 430 Hz at 150mm, 360 Hz near 250 mm, and 320 Hz near 400 mm. Finally, the 3rd harmonic resonant frequency was very close to 450 Hz at 600 mm.

The temperature used for the resonant frequency calculation was higher than the actual combustion chamber temperature due to heat transfer loss and so on. Therefore, it can be predicted that the actual resonance frequency will be lower than the calculated resonance frequency. On the other hand, the resonance frequency up to the exhaust duct was thought to cause little change or slight rise because the room temperature was used. Therefore, the actual crossing point will occur at the length of the combustor shorter than the intersection of Fig. 4.2(a).

Figure 4.3 showed the resonance frequency to the orifice attached to the closed boundary combustor and the resonance frequency to the movable nozzle. At the first harmonic frequency of the two resonant frequencies, there was no intersection. At the 2nd harmonic frequency, an intersection occurred at 330 Hz near 380 mm. An intersection occurred at 510 Hz near 500 mm at the 3rd harmonic frequency. Unlike the condition in Fig.4.2, the two resonant frequencies in Fig.4.3 are the same temperature, so both resonant frequencies were overestimated. Therefore, the actual crossing point will be thought to occur at a slightly lower frequency, although the length of the combustor is similar.

Nevertheless, the possibility of amplification by the resonance frequency was high at the intersection of two resonance frequencies. When the node points of two resonance frequencies matched each other at the intersection conditions, the probability of instability will increase. In addition, the length of the combustor in which the standing waves were formed differs according to each condition.

The probability that the node points coincide different in case of the exhaust duct and

the movable nozzle in Fig. 4.2 will be less than the conditions of the orifice and the movable nozzle because the difference in the length of the standing wave was very large and the intersection of harmonic order was different.

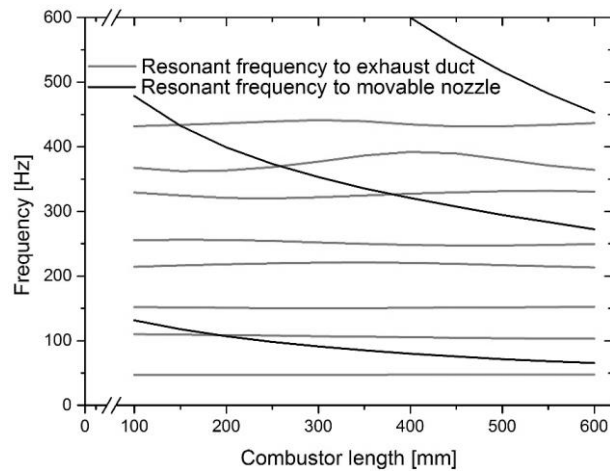


Fig. 4.2 Resonance frequency up to the movable nozzle and the exhaust duct without orifice condition

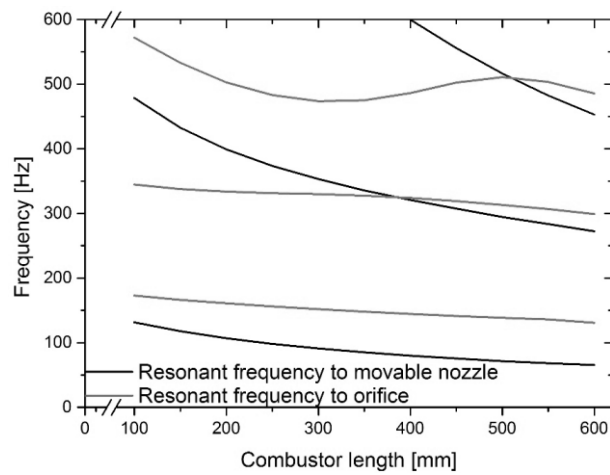


Fig. 4.3 Resonance frequency up to the movable nozzle and the orifice with orifice condition

### **4.3 Effect of the Combustor Length on Velocity and Heat Release**

To determine the effect of the resonant frequency on the flow, the magnitude of the air and fuel velocity perturbations and the magnitude of the heat perturbation perturbations were measured by varying the length of the combustor from 100 mm to 620 mm. At this time, we gave the excitation to the flow through the loudspeaker, and we figured out what kind of change occurred according to the frequency.

First, the standard deviation of the velocity and heat release perturbations was derived to express the effect of the length of the combustor on the excitation frequency in Fig. 4.4. The standard deviations of the velocity and heat release perturbation oscillations that occurred as the combustor length varied from 100 mm to 620 mm were determined. Figure 4.4 (a) showed the standard deviation of air velocity perturbation. At the closed boundary combustor without orifice, little increase of standard deviation at 200 Hz was observed and the standard deviation at 400 Hz increased sharply. On the other hand, when the orifice is mounted on the upper end of the combustor at the closed boundary, a sharp increase of the standard deviation occurred at 200 Hz, and a sharp increase occurred again at 280 and 300 Hz. The standard deviation decreased rapidly at 320 Hz and more. This showed that the air velocity perturbation is greatly affected by the length of the combustor at 400 Hz for closed boundary combustors without orifice and from 200 Hz to 300 Hz when the orifice was added at the closed boundary.

In the case of the fuel velocity perturbation of Fig. 4.4(b), the standard deviation of the velocity perturbation was large when the orifice is present, similarly to the air velocity perturbation. It was similar that the standard deviation at the closed boundary without orifice increased sharply at 400 Hz. It was also similar to show very low values at other frequencies. When the orifice is present at the closed boundary, the peak appeared at 100 Hz and 280 Hz, unlike the air velocity perturbation. The change tendency continued to increase from 320 Hz, which suggests that the next peak will occur near 400 Hz. The range from 200 Hz to 320 Hz, where the second increase or decrease appeared, corresponded to the region where the rapid increase and decrease of the standard deviation of the air velocity



fluctuation occurred.

The standard deviations of the heat release fluctuations were higher at low excitation frequencies unlike air velocity perturbations or fuel velocity perturbations, and tended to decrease as increasing frequency in Fig. 4.4(c). This was the same for closed boundary without orifice and orifice mounting conditions. However, a sharp increase occurred at 400 Hz of the closed boundary without orifice, which was identical to that occurring at the flow velocity perturbation.

The variation tendency of the velocity perturbation based on the excitation frequency was changed at the inflection point of the standard deviation. The air velocity perturbations almost constant with varying lengths of the combustor at closed boundary with orifice when the standard deviations was very low at below 180 Hz and above 360 Hz. The change tendencies from 200 Hz to 260 Hz were similar. For the closed boundary without orifice, a sharp change with varying length of the combustor was observed only at 400 Hz, and little change was observed in the remaining regions.

For velocity perturbations at closed boundary with orifice, the inflection point appeared twice as shown in Fig. 4.4(b). Therefore, a similar change tendency appeared from 80 Hz to 180 Hz based on the inflection point, and a change tendency different from the former occurred in the range of 220 Hz to 300 Hz. Finally, there was another variation trend in the region above 340 Hz. The fuel velocity perturbation of the closed boundary without orifice had a similar tendency to change below 160 Hz and the velocity perturbation was almost constant from 180 Hz to 360 Hz. A new tendency to change appeared at 380 Hz. The rapid change occurred with varying the length of the combustor at 400 Hz.

A large standard deviation meant that the length of the combustor was greatly affected. Figure 4.4 (a) and (b) showed that the resonant frequency did not change much even if the combustion chamber length changed at the closed boundary without orifice. Therefore, resonance frequency of the entire combustor was the main factor, not the resonance frequency up to the movable nozzle where the resonance frequency changed relatively when the nozzle moved in the closed boundary without orifice as assumed in the previous chapter.

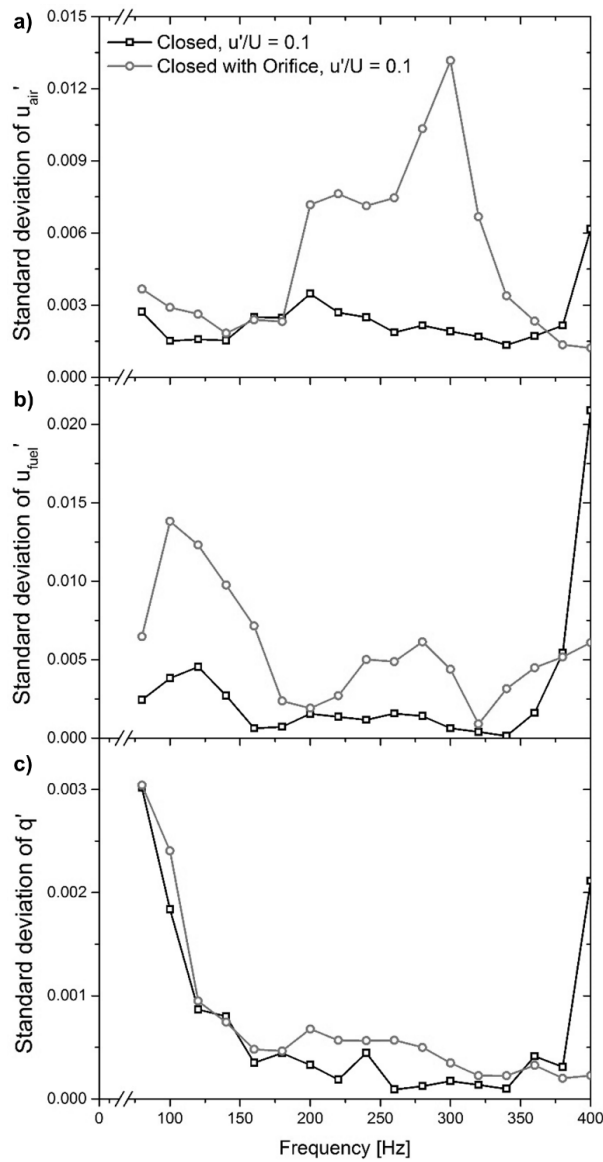


Fig. 4.4 Standard deviation of the (a) air velocity, (b) fuel velocity and (c) heat release perturbations

For the probably unstable conditions inferred from the previous chapter, the standard deviation at the intersections of 600 mm and 450 Hz increased sharply at the closed boundary. The frequency corresponding to the peak could not be confirmed due to the

constraints of the experimental conditions, but it was confirmed that the unstable amplification was observed at the intersection of Fig.4.2. In Fig.4.3, the standard deviation also increased at the intersection of 2nd harmonic resonant frequency. In order to confirm the cause of the length, the change of velocity perturbation with varying the length corresponding to the peak was confirmed.

Figure 4.5 depicted conditions showing the largest change with varying the combustor length in the trend group of air velocity perturbation divided by standard deviation in Fig.4.4. Figure 4.5 (a) showed the condition with or without orifice for the air velocity perturbation. At 300 Hz with the orifice, the greatest change occurred with the largest standard deviation. Under this condition, the peak occurred at 320 mm. This was similar to the intersection point of the 2nd harmonic resonant frequency in Fig.4.3, and it was confirmed that the velocity perturbation occurred due to the resonance frequency. Also, in case of 260 Hz, the frequency became similar to the resonant frequency when the length of the combustor became longer as shown in Fig.4.3. This phenomenon can also be seen in Fig.4.5. At 400 Hz at the closed boundary without orifice, the maximum value was shown at 520 mm, which can also be assumed to occur at the intersection when considering the reduction of the resonant frequency in case of the movable nozzle in Fig.4.2.

Figure 4.5(b) showed the perturbation of heat release under these conditions. In the case of the orifice mounting condition at the closed boundary, the perturbation of the heat release was increased as increasing of the velocity perturbation at 260 Hz. But a completely different tendency to change occurred at 300 Hz. At 400 Hz with the closed boundary without orifice, the heat release increased with increasing velocity perturbation over 240 mm, but the velocity perturbation and the heat perturbation were reversed for those below 400 mm. Therefore, the velocity perturbation was changed due to the resonant frequency, but the perturbation of heat release showed nonlinear characteristics because the heat release oscillation was out of proportion to velocity perturbation.

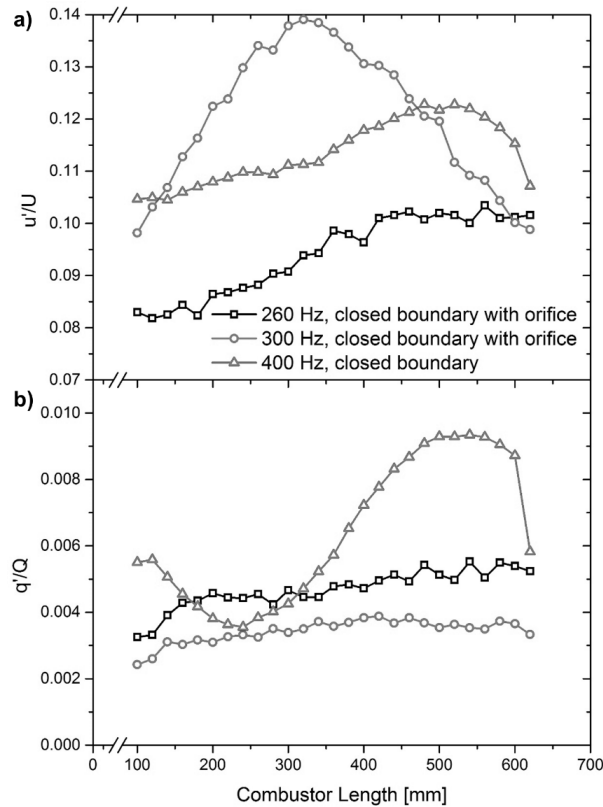


Fig. 4.5 Maximum variation of (a) air velocity and (b) heat release perturbations with varying the combustor length in the each trend group of air velocity perturbation divided by standard deviation

Figure 4.6 showed the peak condition of the fuel velocity fluctuation standard deviation in Fig. 4.4(b) according to the length of the combustor. Figure 4.6 (a) showed the peak condition at the closed boundary without orifice and Fig. 4.6(b) showed the peak condition with the orifice at the closed boundary. The speed of sound of the fuel was faster than that of the air. The flame was present at the top of the fuel nozzle, so the temperature change over the length of the combustor was very large. Therefore, there was a big problem in applying the resonance frequency obtained in Chapter 4.2.

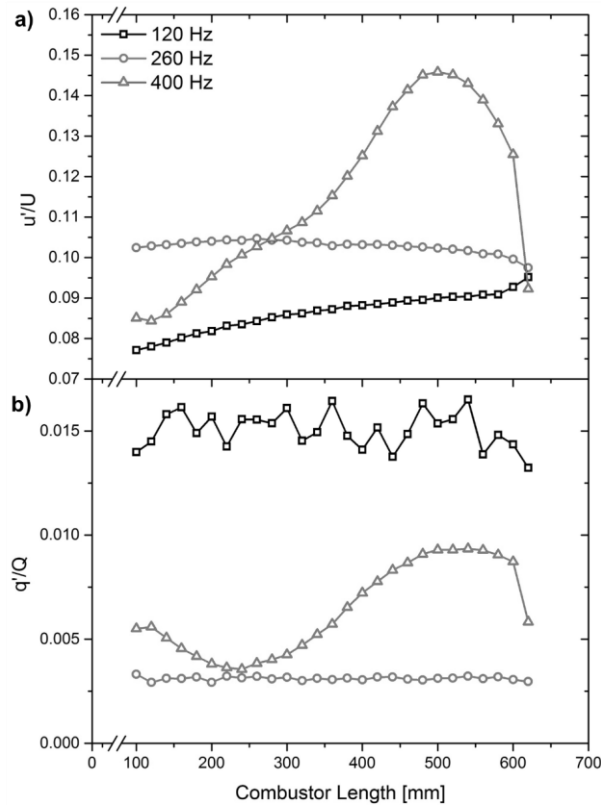


Fig. 4.6 Maximum variation of (a) fuel velocity and (b) heat release perturbations with varying the combustor length in the each trend group of air velocity perturbation divided by standard deviation at the closed boundary without orifice

In the closed boundary combustor without orifice of Fig. 4.6, the fuel velocity perturbation value was increased with increasing combustor length in the lower frequency zone and the value was almost constant in the middle zone, among the three regions divided by the minimum value of the standard deviation. Rapid amplification occurred above 360 Hz. The heat release for this condition was nonlinear except for the region of 400 Hz at 240 mm or more similar to the case of the air perturbation in Fig.4.5.

Figure 4.7 showed the standard deviation peak condition of the fuel velocity for a combustor equipped with an orifice at the closed boundary. At low frequency, the velocity

perturbation increased with the length of the combustor as the result of the closed boundary, but the increase width was much larger. The peak of the middle region appeared near 300mm. The peak occurred near 400mm in the region above 340Hz. In the orifice mounting condition, the heat release showed nonlinear characteristics with the velocity perturbation.

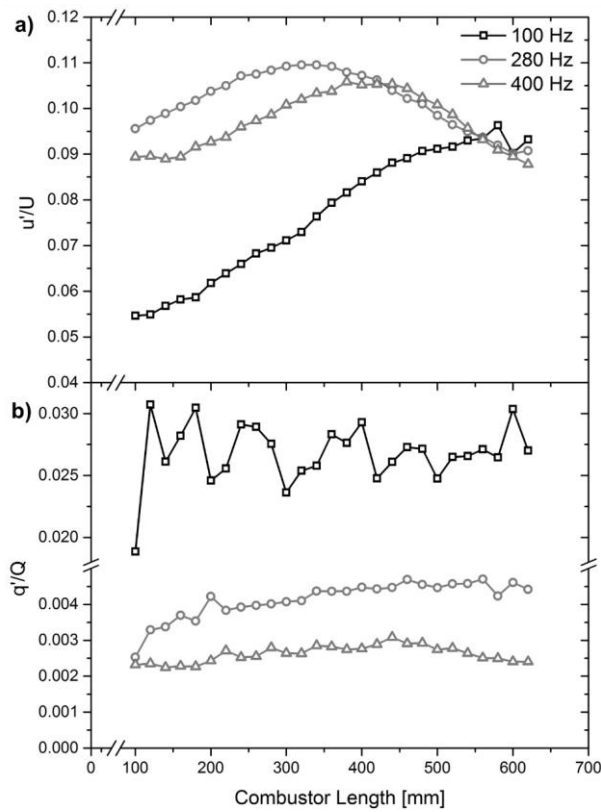


Fig. 4.7 Maximum variation of (a) fuel velocity and (b) heat release perturbations with varying the combustor length in the each trend group of air velocity perturbation divided by standard deviation at the closed boundary with orifice

#### 4.4 Comparison between Open and Closed Boundary Results

The heat release of open boundary, closed boundary without orifice and closed boundary with orifice by using the flame transfer function concept was compared for same combustion chamber length as shown in Fig.4.8. First, when the closed boundary without orifice was formed, the perturbation of heat release versus velocity perturbation increased sharply in the low frequency region below 100 Hz. After that, the perturbation of heat release decreased rapidly and then started to increase again from 260 Hz. On the other hand, the response of the heat release in the combustor including the orifice at the closed boundary was very low at 80 Hz. The gain of the flame transfer function of the closed boundary with orifice became similar to the gain of the open boundary at 100 Hz. Thereafter, the gain of the flame transfer function tended to decrease with increasing excitation frequency. We had considered the effect of harmonics as described in chapter 3.5.2 on this trend of change.

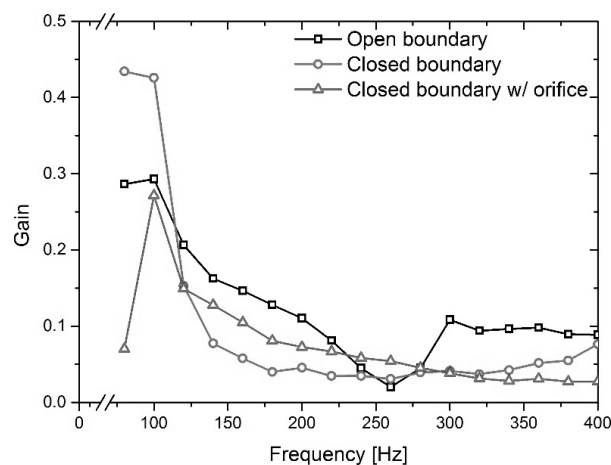


Fig. 4.8 Heat release of open boundary, closed boundary without orifice and closed boundary with orifice by using the flame transfer function concept with 500 mm combustion chamber length

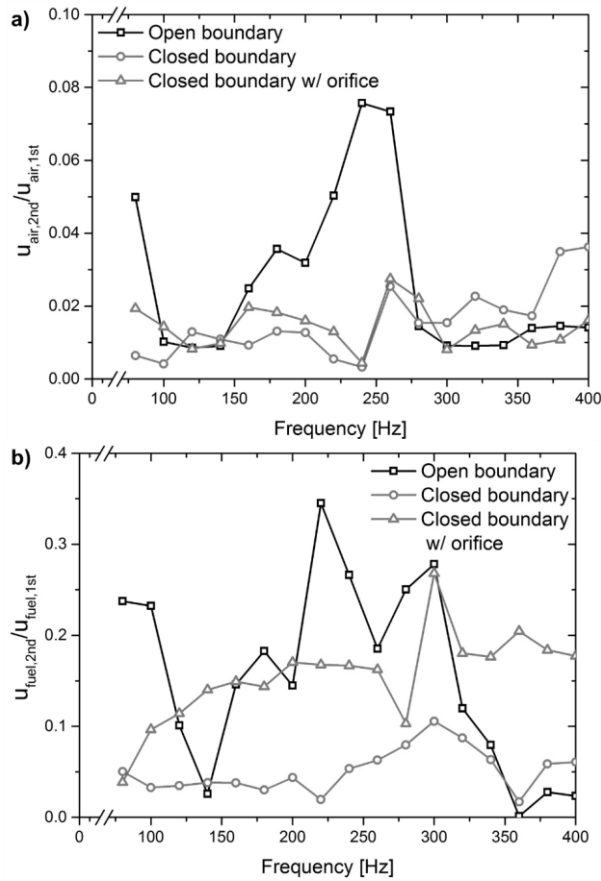


Fig. 4.9 Ratio of 1st harmonic velocity and 2nd harmonic velocity of (a) air and (b) fuel with the open boundary, the closed combustor boundary without orifice and the closed boundary with orifice

Figure 4.9 showed the ratio of 1st harmonic velocity and 2nd harmonic velocity according to the open boundary and the presence or absence of orifice in closed combustor boundary. Fig.4.10 showed the ratio of heat release rate. First, the ratio of air velocity perturbation in Fig. 4.9(a) decreased as the closed boundary was formed, and the effect of orifice occurred only in the region above 300 Hz. The ratio of the fuel velocity perturbations in Fig.4.9 (b) also decreased as the closed boundary is formed, but, the magnitude of the 2nd harmonic decreased sharply to be close to the size of the closed boundary condition at



the open boundary in the region above 300 Hz. On the other hand, due to the orifice effect, the 2nd harmonic of fuel velocity oscillation remained large and the ratio of 1st harmonic and 2nd harmonic fuel velocity still maintained more than 20% in spite of decreasing harmonic velocity ratio in the region of 300 Hz and above.

Similar to the resemblance between the velocity perturbation of the open and closed boundaries at 300 Hz, the ratio of the heat release perturbations also remained similar at 300 Hz and over as shown in Fig.4.10. As shown in Chapter 3.4.2, the ratio of 2nd harmonic abruptly increased at 260 Hz, in which the gain of the flame transfer function dropped sharply at the open boundary. However, such a sudden change did not occur at the closed boundary. This phenomenon can be associated with no abrupt decrease of the gain.

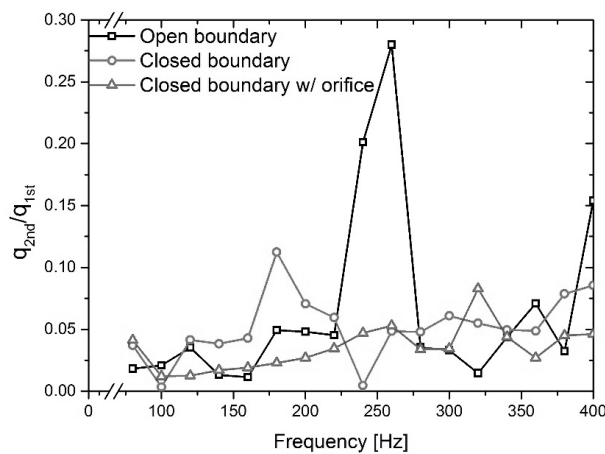


Fig. 4.10 Ratio of 1st harmonic velocity and 2nd harmonic velocity of heat release with the open boundary, the closed combustor boundary without orifice and the closed boundary with orifice

The formation of closed boundaries in the combustor reduced the harmonic effect on the air. In addition, the orifice at the end of the combustor showed a slight increase below 260 Hz and a slight decrease above 260 Hz. The effect on the fuel flow was reduced due to the closed boundary, but the overall increase was caused by the orifice. Also, in the region above 320 Hz, the harmonic effect was larger than the open boundary when the orifice was

installed. The heat release rate was drastically changed at 260 Hz at the open boundary, but it was maintained at a rate of less than 10% at the closed boundary. In addition, when the orifice was installed, sudden change was reduced and became into gradual change tendency.

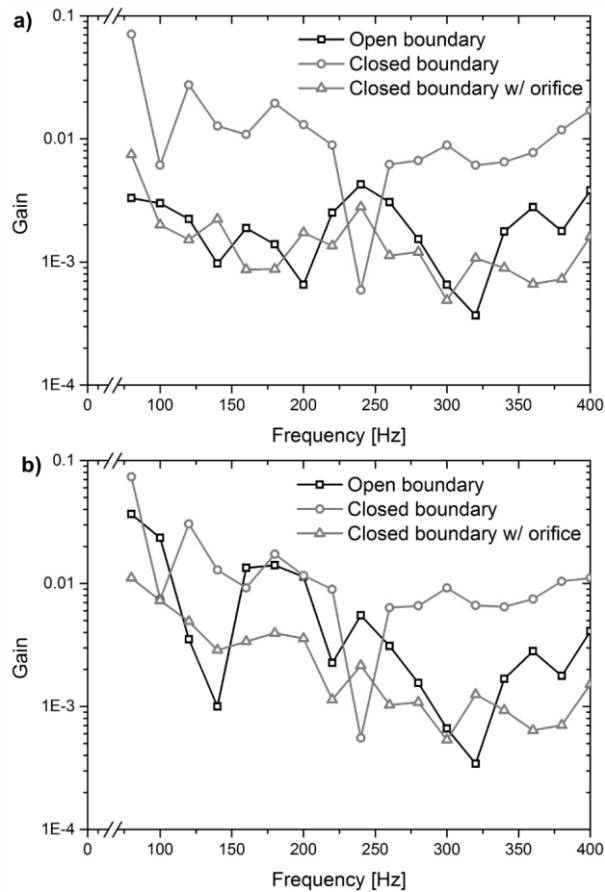


Fig. 4.11 2nd harmonic flame transfer function based on the perturbation of the (a) air velocity and (b) fuel velocity by using Eqn. (3)

Figure 4.11 showed the 2nd harmonic flame transfer function by using Eqn. (3). Like the open boundary, the 2nd harmonic velocity of the fuel and air were varied, so the each flame transfer function was different. At this time, the gain of the closed boundary with the

orifice was similar to the gain of the open boundary, and only the gain of the closed boundary without orifice showed a distinct tendency. Therefore, the 1st harmonic excitation of the velocity perturbation of the fuel or air influenced the 2nd harmonic oscillation at the open boundary, and the 2nd harmonic velocity perturbation affected the heat release oscillation, but the 1st harmonic excitation of the fuel or air velocity perturbations directly affected the 2nd harmonic heat release perturbation at the closed boundary without orifice.

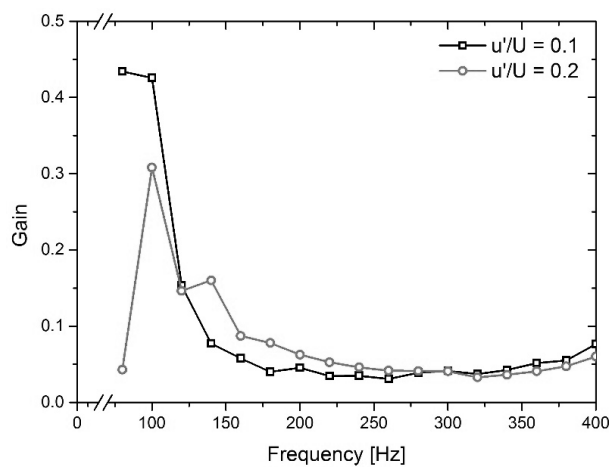


Fig. 4.12 The nonlinearity of the heat release perturbation to the velocity perturbation at the closed boundary without orifice

The nonlinearity of the heat release perturbation to the velocity perturbation at the closed boundary without orifice was confirmed in Fig. 4.12. In Fig.3.21 (a), the nonlinear characteristics of the open boundary were very weak, while the nonlinearity of the closed boundary without orifice was very strong in the low frequency domain. Therefore, it can be seen that both the nonlinear characteristic of the harmonic effect and the nonlinear characteristic of the velocity perturbation were strengthened when the closed boundary without orifice was formed.

## **4.5 Relation with the Combustor Instability Characteristics**

Figure 4.13 and 4.14 showed the fluctuation of the dynamic pressure in the combustion chamber according to the length of the combustor in the closed boundary combustor where the orifice exists. When the orifice did not exist, the pressure oscillation showed the very low magnitude. Figure 4.13 showed the dynamic pressure variation from 100mm to 350mm with 50mm interval and Fig.4.14 showed the dynamic pressure with 50mm interval from 400mm to 600mm. There was a difference in magnitude of the dynamic pressure with combustor length variation from 100 mm to 600 mm, but a peak occurred. However, when the length of the combustor was 350 mm, the pressure perturbation increased from 240 Hz, and the pressure perturbation was maintained at the certain level from 250 Hz to 300 Hz, and then decreased to 330 Hz.

Figure 4.15 showed the voltage measured by a hot wire anemometer when the speaker had a random frequency to obtain the resonant frequency of the air supply tube. The first peak occurred at a very narrow range at 17.6 Hz and the second peak occurred at a wide range centered at 186.4 Hz. Thereafter, very small peaks occurred at 578.6 Hz and 780 Hz. This allowed the air tube to amplify the perturbation when the external perturbation is 17.6 Hz and also amplifies the perturbation when the air flow perturbation occurred around 186.4 Hz.

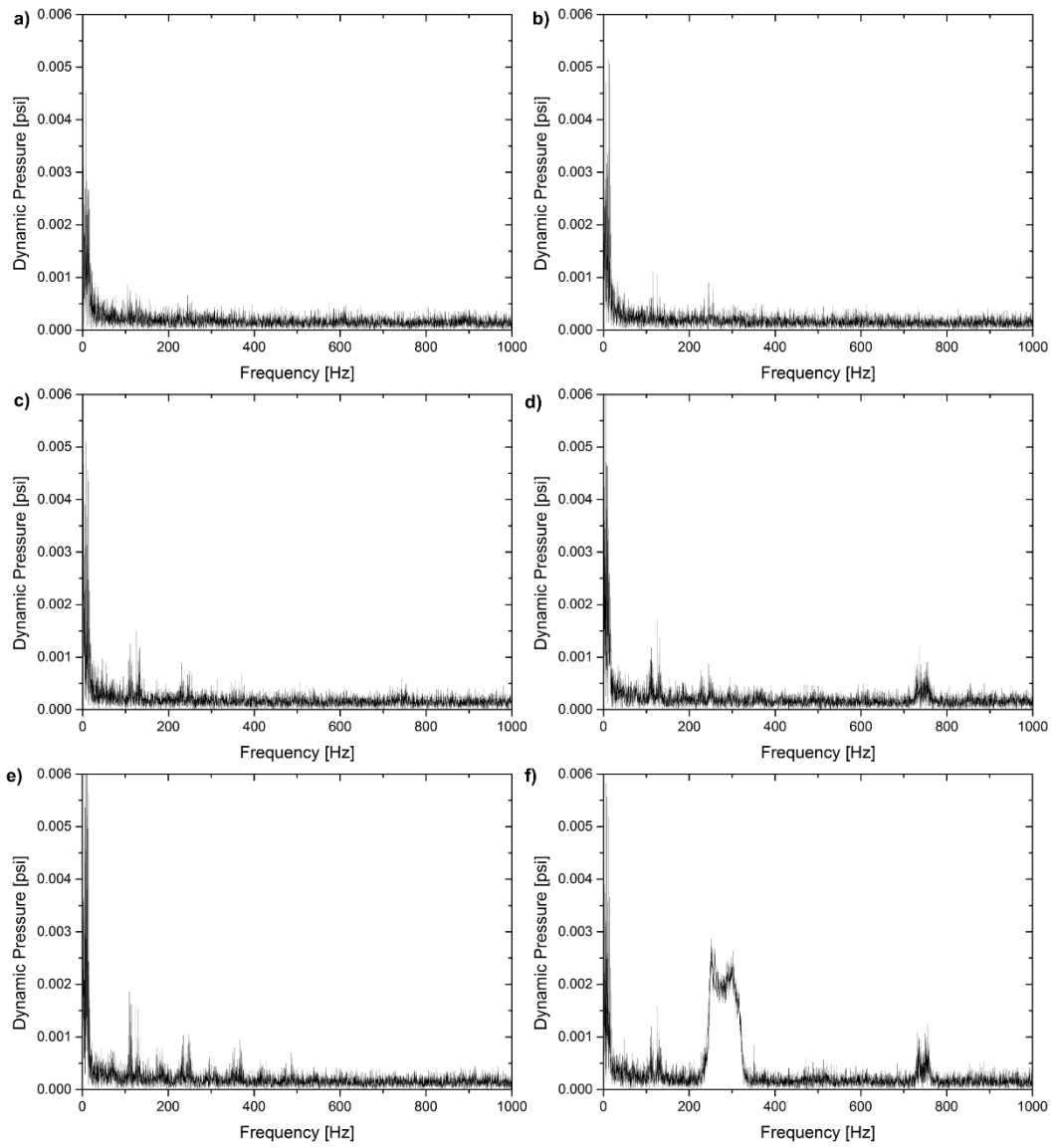


Fig. 4.13 Dynamic pressure in the combustion chamber in the closed boundary combustor with orifice at the (a) 100 mm, (b) 150 mm, (c) 200 mm, (d) 250 mm, (e) 300 mm and (f) 350 mm length of the combustor

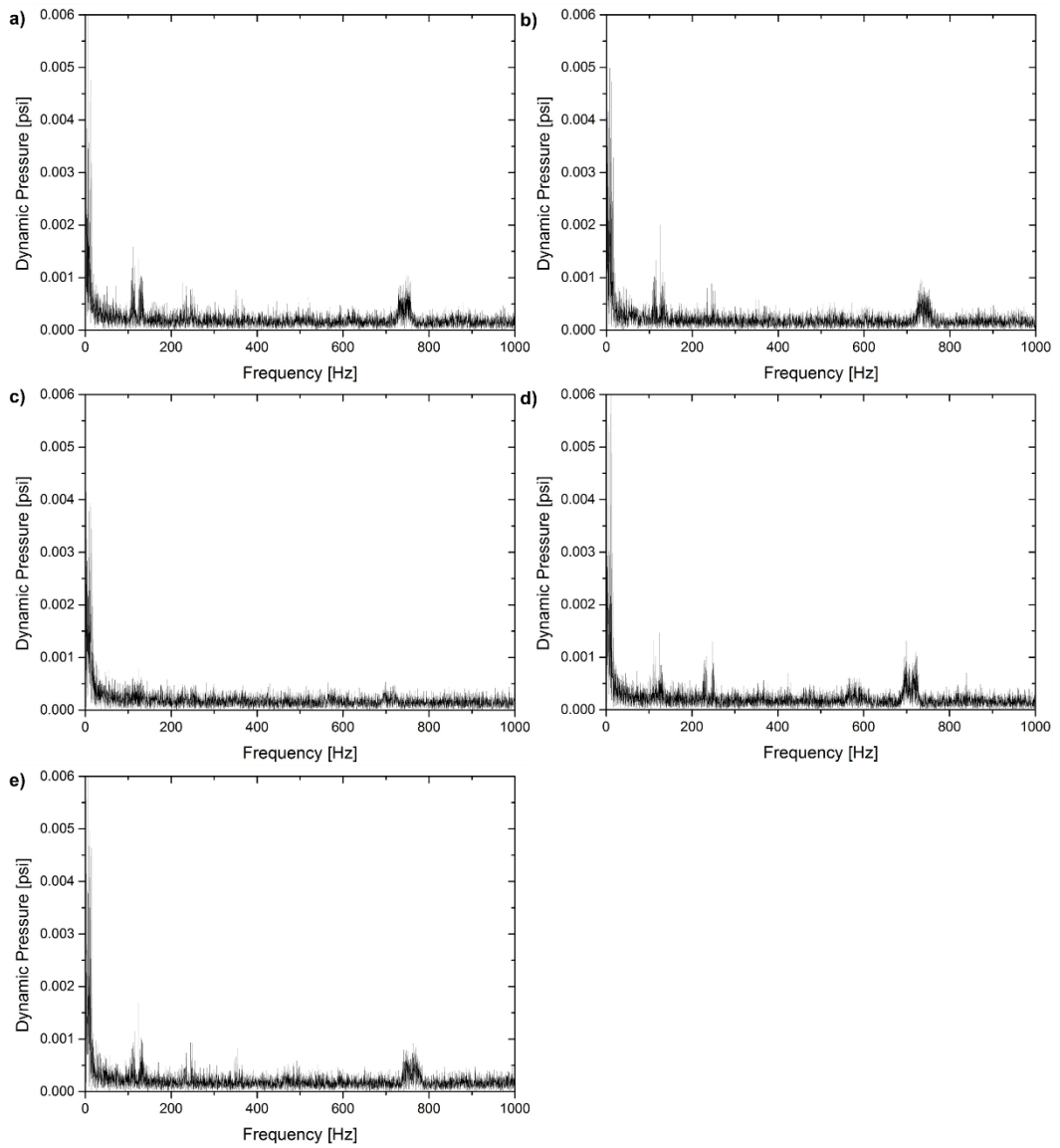


Fig. 4.14 Dynamic pressure in the combustion chamber in the closed boundary combustor with orifice at the (a) 400 mm, (b) 450 mm, (c) 500 mm, (d) 550 mm, (e) 600 mm length of the combustor

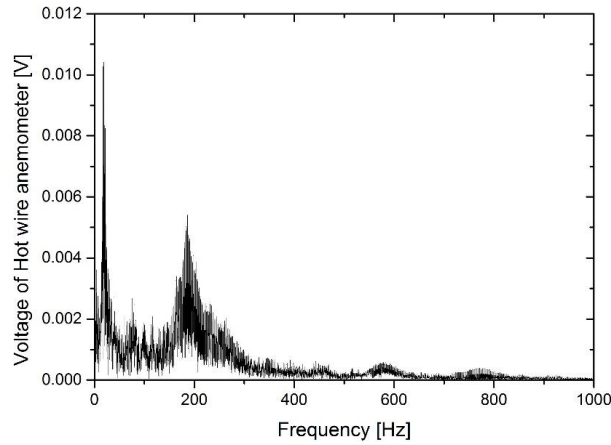


Fig. 4.15 Voltage measured by a hot wire anemometer located at the air supply tube with a random frequency

Figure 4.16 showed the change of the fuel and air velocity perturbation as a function of frequency when there was an excitation in a 350 mm combustor condition where pressure perturbation was strong. The magnitude of the air perturbation increased from 260 Hz to 340 Hz, and increased the most at 300 Hz. In the case of fuel velocity perturbation, the overall value was low but slightly increased at 280 Hz. The influence of the flame transfer function of Fig. 3.19 existed on the basis of this change. Not only the gain of the flame transfer function started to increase again from 260 Hz, but also there were various phase differences at 300 Hz. It is known that when phase difference is  $180 \pm 90^\circ$ , destructive interference occurs and constructive interference occurs at  $0 \pm 90^\circ$ . The phase difference between the velocity perturbation and the heat release perturbation in Fig. 3.19(b) belonged mostly to the destructive interference region and only to the region corresponding to the constructive interference only when the velocity perturbation was low at 300 Hz. Therefore, a low velocity perturbation at 300 Hz was required for heat release perturbation to cause constructive interference with velocity perturbation.

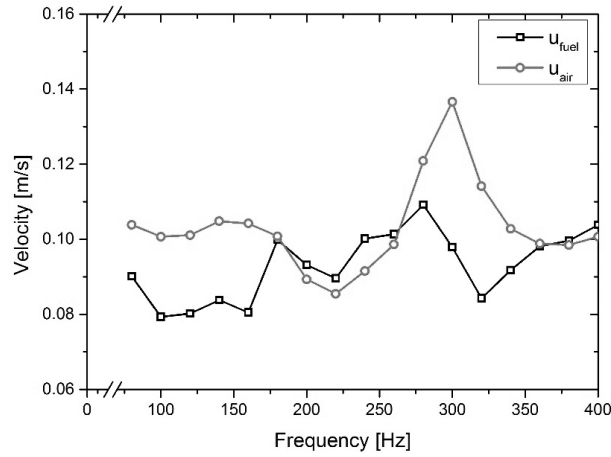


Fig. 4.16 Air and fuel velocity perturbation as a function of frequency at the 350 mm length of the combustor with external excitation

Combining the results in Fig. 4.15 and Fig. 4.16, the cause of the instability shown in Fig. 4.13(f) can be determined. The resonant frequency of the air pipe increased the air velocity perturbation to 300 Hz with maximum magnitude at 180 Hz as shown in Fig. 4.15. Also, when the length of the combustor is from 300 mm to 350 mm, the resonance frequency had the greatest influence on the air velocity and the frequency most affected by the resonance was 300 Hz as shown in Fig. 4.4 and Fig. 4.5.

Therefore, considering the frequency from 260 Hz to 340 Hz, which was the region where the velocity perturbation can increase according to the length of the combustor, and the region of 300 Hz or less where the amplification occurred due to the resonance frequency of the air pipe, it corresponded to the pressure perturbation frequency from 250 Hz to 300 Hz in Fig. 4.13(f). Especially, the influence of the air pipe decreased as decreasing the frequency in the region of below 300 Hz, and the effect on the length of the combustor increased as increasing the frequency when the oscillation frequency was 300 Hz or less. The pressure perturbation in which a similar magnitude was maintained occurred from 250 Hz to 300 Hz by combining these two influences.



## CHAPTER 5

### CONCLUSION

This study investigated the dynamic characteristics at the open combustor boundary and the closed boundary in the Burke-Schumann flame. Also, the effect of the exhaust duct was determined by installing an orifice at the end of the closed boundary combustor. The pressure perturbation in the combustion chamber was analyzed in relation to the dynamic characteristics.

In the open boundary combustor, this study presents the results for the flame response of a diffusion flame with acoustic forcing. The flame surface, flame length, and heat release oscillations are measured to obtain an experimental analysis of the flame response. The flame transfer function is measured for a diffusion flame and a premixed flame. The experimental results are then compared with the analytical solution. The flame length decreases with acoustic forcing because of enhanced mixing. The forcing frequency is an important factor for determining the flame shape and flame length, whereas the mean input velocity has no significant effect on the flame length. The flame length has a minimum value when the forcing frequency is the resonant frequency of the air line. The flame length is similar to the non-forcing length when the forcing frequency exceeds the specific frequency, which is 200 Hz in this study. The rate of length change is more sensitive to force when the fuel has less mass diffusivity. For the analytical solution, the flame length is constant regardless of the forcing conditions. A local stagnation of the flame propagation and flame cutting occur with low-frequency forcing. The flame cuts where the OH signal is stagnant. The flow is divided into upward and downward flows with the stagnation point as the center. This separation makes the flame cut. The flame shape and the wavelength of flame surface undulations depend on the Strouhal number. The magnitude of flame surface undulations depends on the Peclet number. This dependence on the Peclet number is similar to the analytical results. The diffusion and premixed flames react like low-pass filters according to the results of the Strouhal number's dependence on the flame surface, similar

to the analytical solution. The condition with a low magnitude of the flame transfer function corresponds to the condition of a flame surface with less oscillation. The magnitude of the flame response is related to the flame surface oscillations. The gain of the flame transfer function is similar with the oscillation magnitude of the flame area except for flame cutting conditions. The analytical solution that shows a changing tendency of the flame transfer function is well fitted with the experimental results.

Next, we investigated the effects of the average velocity and mass diffusion coefficient, which are constituents of the Péclet number on the shape of the flame and the perturbation of heat release. An experiment was performed by changing the velocity perturbations, which are known to affect flame shape and heat release perturbations. In the case of the flame shape, the change of the average velocity affected the magnitude of the flame shaping, and when the fuel composition changed, the shape changed on account of soot occurring from incomplete combustion. Changes in velocity perturbations affected the number of waves that constituted the flame. The gain of the flame transfer function did not change the tendency of the change; rather, it decreased the magnitude slightly with the increasing input average velocity. When the methane ratio in the fuel increased, the magnitude of gain decreased and the frequency of the gain was the least increased. In addition, the influence of the condition change was larger when the relation between the Strouhal number and the gain was considered with the flame length. The gain was more sensitive to the change of the Strouhal number at the high Péclet number when the Péclet number was changed by varying the average velocity. Nonetheless, the gain was more sensitive to the Strouhal number at the low Péclet number when the fuel composition affected the Péclet number.

In the case of the phase difference, the average velocity increase caused a decrease in the overall phase difference. Increasing the methane ratio in the fuel composition decreased the phase difference at the low frequency range and increased the frequency at which the rapid change of magnitude occurred. In the measurement of the flame transfer function through the change of the velocity perturbation, a slight decrease of the gain occurred with a larger velocity perturbation, and the phase difference was constant except for 300 Hz. In the theoretical results of the literature, the change of the flame shape and flame transfer

function was shown when the Péclet number was changed. However, it was confirmed through experiments that the flame shape and flame transfer function changed in different ways depending on the method of changing the Péclet number. Therefore, to understand the effects of the combustion condition on the Burke-Schumann flame dynamics, the input velocity and mass diffusivity non-dimensionalized by the Péclet number in analytical studies should be considered separately. Although the forcing frequency varies slightly depending on the experimental conditions, the minimum gain of the flame transfer function appears near 280Hz. This phenomenon occurs because the velocity disturbances do not make the burning area perturbations.

The nonlinear characteristics at the open boundary were roughly divided into two types. First type was the relationship between velocity perturbation and heat release. The flame transfer function basically included the assumption that the velocity perturbation and heat release perturbation are linear. In the case of the gain of the flame transfer function with various value of the velocity perturbation, the larger the velocity perturbation was, the lower the gain was until 260 Hz. The lowest value was reached at 260 Hz. Then, the gain was restored again, and the response was slightly large when the velocity perturbation was small, but the similar magnitude was obtained at the frequency of 360 Hz or more. The phase difference showed almost the same value except for 300 Hz. At 300 Hz, the phase perturbation gradually decreased from 0.1 m/s to 0.2 m/s and the phase difference did not change from 0.2 m/s to 0.25 m/s. Through the flame transfer function, the velocity perturbation and heat release perturbation were nonlinear in the range of from 80 Hz to 400 Hz and from 0.1 m/s to 0.2 m/s. Next, we investigated the effect of 1st harmonic excitation on 2nd harmonic oscillation. Air and fuel were affected differently. Air flow showed the same tendency of change of fuel composition or velocity perturbation magnitude, but it changed its value. However the tendency of change was varied in fuel flow. The heat release ratio of 2nd harmonic and 1st harmonic was the highest at the point where gain was lowest in the flame transfer function. That is, the lower the flame transfer function, the larger the 2nd harmonic heat release. The gain of the 2nd harmonic flame transfer function also varied according to the fuel and air velocity fluctuation magnitudes, and the nonlinear

characteristics were different according to the velocity perturbation magnitude.

The influence of the resonance frequency was confirmed and the relationship between the resonance frequency and the pressure perturbation was determined on the closed boundary. When the resonance frequency was calculated, the bottom of the air tube was set at one end and the opposite end was set at the moving nozzle, the end of the combustion chamber, and the exhaust duct according to the condition of the combustor. In order to minimize the effect of the exhaust duct, the orifice was mounted at the end of the combustion chamber and the resonant frequency was calculated for these conditions. The effect of the resonance frequency was identified by determining the intersection of two types of resonance frequencies that might affect the flow in the combustor chamber. At the closed boundary without orifice, the intersection of the resonance frequency to the exhaust duct and the resonance frequency to the movable nozzle was confirmed. When the orifice was installed at the closed boundary, the intersection of the resonance frequency to the orifice and the resonance frequency to the movable nozzle was determined. At the closed boundary without orifice, intersections had occurred at 200 mm with 100 Hz, 150 mm with 430 Hz, 250 mm with 360 Hz, 400 mm with 320 Hz, and 600 mm with 450 Hz. In the case of an orifice mounted at the closed boundary, the intersection occurred at 380 mm with 330 Hz and 500 mm with 510 Hz. In order to check whether the actual instability occurred under the condition that the resonance frequency crossed, the change of the velocity perturbation was measured by varying the length of the combustor with the external excitation.

At the intersection of the resonant frequencies, the velocity perturbation at 600 mm with 450 Hz of the closed boundary without orifice was abruptly changed, and the velocity perturbation changed at 380 mm with 330 Hz under the condition of the orifice. The standard deviations of the velocity perturbations also grouped according to the change trends of the velocity perturbations. In the case of small standard deviation, the velocity perturbation did not change with the length of the combustor, and the velocity perturbation tended to increase with increasing combustor length at low frequency. In the remaining conditions, the velocity perturbation increased with the increase of the length of the

combustor, then decreased again. When the velocity perturbation changed according to the length of the combustor, the heat release perturbation showed a nonlinearity with the velocity perturbation except for a part of 400 Hz. When the length of the combustor was changed from 100 mm to 600 mm at intervals of 50 mm, a pressure perturbation occurred at 350 mm of the closed boundary condition equipped with the orifice. The pressure perturbation occurred from 250 Hz to 300 Hz. This condition was a condition that affected both the resonance frequency of the air tube and the resonance frequency of the combustor, which was explained by the change of velocity perturbation according to the length of the combustor.

The effect of the flame dynamic characteristics on the open boundary was largely affected by the fuel composition and the nonlinearity occurring at the 2nd harmonic frequency. At the closed boundary, the resonant frequency of the combustor caused a change in the velocity perturbation, and the magnitude and phase difference of the flame transfer function also affected the change in the velocity perturbation. The combination of the resonant frequency of the combustor and the air supply line caused pressure perturbations without external disturbances. This pressure perturbation mechanism may be used to understand combustion instability phenomena.

## REFERENCES

- [1] N. Magina, Dynamics of Harmonically Forced Nonpremixed Flames, Ph.D THESIS, 2016.
- [2] S. Ducruix, D. Durox and S. Candel, Theoretical and experimental determinations of the transfer function of a laminar premixed flame, Proceedings of the Combustion Institute 28 (2000), 765-773.
- [3] T. Schuller, D. Durox and S. Candel, A unified model for the prediction of laminar flame transfer functions: comparisons between conical and V-flame dynamics, Combustion and Flame 134 (2003), 21-34.
- [4] D. Durox, T. Schuller, and S. Candel, Combustion Dynamics of Inverted Conical Flames, Proceedings of the Combustion Institute 30 (2005), 1717-1724.
- [5] K. Kim, J. Lee, B. Quay and D. Santavicca, Response of partially premixed flames to acoustic velocity and equivalence ratio perturbations, Combustion and Flame 157 (2010), 1731-1744.
- [6] B. Bellows, M. Bobba, A. Forte, J. Seitzman and T. Lieuwen, Flame transfer function saturation mechanisms in a swirl-stabilized combustor, Proceedings of the Combustion Institute 31 (2007), 3181–3188.
- [7] W. Polifke and C. Lawn, On the low-frequency limit of flame transfer functions, Combustion and Flame 151 (2007), 437–451.
- [8] D. Kim, J. Lee, B. Quay, D. Santavicca, K. Kim and S. Srinivasan, Effect of flame structure on the flame transfer function in a premixed gas turbine combustor, Journal of Engineering for Gas Turbines and Power 132 (2010), 021501.
- [9] P. Palies, T. Schuller, D. Durox, and S. Candel, Modeling of premixed swirling flames transfer functions, Proceedings of the Combustion Institute 33 (2011), 2967-2974.
- [10] N. Noiray, D. Durox, T. Schuller, and S. Candel, Self-induced Instabilities of Premixed Flames in a Multiple Injection Configuration, Combustion and Flame 145 (2006), 435-336.

- [11] N. Noiray, D. Durox, T. Schuller and S. Candel, A unified framework for nonlinear combustion instability analysis based on the flame describing function, *Journal of Fluid Mechanics* 615 (2008), 139-167.
- [12] K. Balasubramanian and R. Sujith, Nonlinear response of diffusion flames to uniform velocity disturbances, *Combustion Science and Technology* 180 (2008), 418–436.
- [13] K. Balasubramanian and R. Sujith, Non-normality and nonlinearity in combustion–acoustic interaction in diffusion flames, *Journal of Fluid Mechanics* 594 (2008), 29–57.
- [14] N. Magina, D. Shin, V. Acharya and T. Liewen, Response of non-premixed flames to bulk flow perturbations, *Proceedings of the Combustion Institute* 34 (2013), 963–971.
- [15] N. Magina, V. Acharya, T. Sun and T. Liewen, Propagation, dissipation, and dispersion of disturbances on harmonically forced, non-premixed flames, *Proceedings of the Combustion Institute* 35 (2015), 1097–1105.
- [16] N. Magina and T. Liewen, Effect of axial diffusion on the response of diffusion flames to axial flow perturbations, *Combustion and Flame* 167 (2016), 395-408.
- [17] Z. Yao and M. Zhu, A distributed transfer function for non-premixed combustion oscillations, *Combustion Science and Technology* 184 (2012), 767–790.
- [18] S. Farhat, D. Kleiner and Y. Zhang, Jet diffusion flame characteristics in a loudspeaker-induced standing wave, *Combustion and Flame* 142 (2005), 317-323.
- [19] Q. Wang, H. Huang, H. Tang, M. Zhu and Y. Zhang, Nonlinear response of buoyant diffusion flame under acoustic excitation, *Fuel* 103 (2013), 364-372.
- [20] T. Liewen, Nonlinear kinematic response of premixed flames to harmonic velocity disturbances, *Proceedings of the Combustion Institute* 30 (2005), 1725-1732.
- [21] K. Kim, Nonlinear Interactions between the Fundamental and Higher Harmonics of Self-Excited Combustion Instabilities, *Combustion Science and Technology* 189 (2017), 1091-1106.
- [22] J. Yoon, S. Joo, J. Kim, M. Lee, J. Lee and Y. Yoon, Effects of convection time on

- the high harmonic combustion instability in a partially premixed combustor, *Proceedings of the Combustion Institute* 36 (2017), 3753-3761.
- [23] A. Orchini and M. Juniper, Flame Double Input Describing Function analysis, *Combustion and Flame* 171 (2016), 87-102.
- [24] M. Kim, J. Yoon, J. Oh, J. Lee and Y. Yoon, An experimental study of fuel-air mixing section on unstable combustion in a dump combustor, *Applied Thermal Engineering* 62 (2014), 662-670.
- [25] J. Seitzman, A. Ungut, P. Paul and R. Hanson, Imaging and characterization of OH structures in a turbulent nonpremixed flame, *Proceedings of Combustion Institute*, 23 (1990), 637-644.
- [26] S. Turns, *An Introduction to Combustion*, McGraw-Hill, 1996.
- [27] M. Stöhr, C. Arndt and W. Meier, Effects of Damköhler number on vortex-flame interaction in a gas turbine model combustor, *Proceedings of the Combustion Institute* 34 (2013), 3107-3115.
- [28] M. Stöhr, I. Boxx, C. Carter and W. Meier, Dynamics of lean blowout of a swirl-stabilized flame in a gas turbine model combustor, *Proceedings of the Combustion Institute* 33 (2011), 2953-2960.
- [29] I. Boxx, M. Stöhr, C. Carter and W. Meier, Temporally resolved planar measurements of transient phenomena in a partially pre-mixed swirl flame in a gas turbine model combustor, *Combustion and Flame* 157 (2010), 1510-1525.
- [30] P. Petersson, R. Wellander, J. Olofsson, H. Carlsson, C. Carlsson, B.B. Watz, N. Boetkjaer, M. Richter, M. Aldén and L. Fuchs, Simultaneous high-speed PIV and OH PLIF measurements and modal analysis for investigating flame-flow interaction in a low swirl flame, *International Symposium Applied Laser Technical Fluid Mechanical* (2012), 09-12.
- [31] P. Xavier, A. Vandael, G. Godard, B. Renou, F. Grisch, G. Cabot, M.A. Boukhalfa and M. Cazalens, Analysis of the flame structure in a trapped vortex combustor using low and high-speed OH-PLIF, *ASME Turbo Expo 2014: Turbine Technical Conference and Exposition* (2014), V04AT04A012-V004AT004A012.



- [32] J. Dawson, R. Gordon, J. Kariuki, E. Mastorakos, A. Masri and M. Juddoo, Visualization of blow-off events in bluff-body stabilized turbulent premixed flames, *Proceedings of the Combustion Institute* 33 (2011), 1559-1566.
- [33] N.A. Worth and J.R. Dawson, Cinematographic OH-PLIF measurements of two interacting turbulent premixed flames with and without acoustic forcing, *Combustion and Flame* 159 (2012), 1109-1126.
- [34] S. Hammack, S. Kostka, A. Lynch, C. Carter and T. Lee, Simultaneous 10-kHz PLIF and chemiluminescence imaging of OH radicals in a microwave plasma-enhanced flame, *IEEE Transactions on Plasma Science* 41 (2013), 3279-3286.
- [35] P.M. Allison, Y. Chen, M. Ihme and J.F. Driscoll, Coupling of flame geometry and combustion instabilities based on kilohertz formaldehyde PLIF measurements, *Proceedings of the Combustion Institute* 35 (2015), 3255-3262.
- [36] S. Meares, V.N. Prasad, M. Juddoo, K.H. Luo and A.R. Masri, Simultaneous planar and volume cross-LIF imaging to identify out-of-plane motion, *Proceedings of the Combustion Institute* 35 (2015), 3813-3820.
- [37] M. Kim, Y. Choi, J. Oh and Y. Yoon, Flame–vortex interaction and mixing behaviors of turbulent non-premixed jet flames under acoustic forcing, *Combustion and Flame* 156 (2009), 2252–2263.
- [38] C. Wilke, A viscosity equation for gas mixtures, *The Journal of Chemical Physics* 18 (1950), 517–519.
- [39] K. Lakshminarasimhan, N. Clemens and O. Ezekoye, Characteristics of strongly-forced turbulent jets and non-premixed jet flames, *Experiments in Fluids* 41 (2006), 523–542.

## 초 록

연소불안정의 정확한 발생 메커니즘은 아직 밝혀지지 않았으나 반응물의 유동 섭동, 열방출량 섭동, 연소실의 음향학적 경계에 의한 섭동이 어떠한 상호 작용을 하는가에 따라 발생 유무가 결정된다고 알려져 있다. 위의 세 가지 섭동이 양적 피드백 루프(positive feedback loop)를 형성하면 연소불안정이 발생할 확률이 높아지며 반대로 음성 피드백 루프(negative feedback loop)를 형성하면 연소불안정 발생 확률이 낮아지는 것으로 알려져 있다. 연소불안정의 위험을 낮추기 위해서 앞에서 말한 대로 연소불안정이 발생하는 조건을 파악하는 것이 필요하다. 연소불안정이 발생하는 조건을 파악하기 위한 기본은 화염의 동특성에 대한 연구를 진행하는 것이다.

본 연구에서는 메탄과 수소의 혼합기체로 이루어진 non-premixed jet flame의 특별한 case 인 Burke-Schumann flame에 대한 동특성 연구를 수행하였다. 화염의 동특성을 외부에서 교란을 발생시켰을 때 열방출량 섭동, 화염 형상을 통해 나타내었다. 화염이 열린 경계에 있을 때 열방출량 및 화염 형상을 계측하여 외부 교란에 대한 화염의 응답 특성을 나타내었다. 화염이 닫힌 경계에 있을 때 실험 장치의 공진주파수를 구하여 이에 대한 영향을 파악하고 self-excited pressure oscillations에 대한 원인을 분석하였다.

열린 경계의 화염의 형상은 크게 3가지로 나타났다. 저주파 영역에서는 화염 형상이 한 주기의 파동 형태로 노즐에 부착되어 있었으며, 그 이상의 영역에서는 화염이 끊어졌다. 또한 250 Hz 근방의 영역에서는 화염이 거의 떨리지 않았으며, 나머지 영역에서는 여러 개의 파동으로 구성된 화염 형상이 나타났다. 화염전달함수도 화염이 떨리지 않는 지점에서 매우 낮은 값을 보였으며 일정 주파수 이상에서 일정한 값으로 유지되었다. 화염전달함수의 응답 값과 화염 면적의 떨림은 화염이 끊어지는 영역을 제외하면 비슷한 변화 경향을 보였다. 열린 경계의 화염은 속도 섭동 크기에 열방출량이 대체적으로 비

레하는 선형적인 관계를 보였으나, 가진주파수의 2nd harmonic frequency로 미치는 영향은 크게 발생하였다. 특히 화염전달함수가 낮게 나타나는 가진주파수나 연료 조성에서 열방출량의 2nd harmonic frequency의 비율이 급격히 증가하였다.

닫힌 경계에서는 공진주파수의 영향을 파악하였다. 비록 movable nozzle로 닫힌 경계를 형성하였지만 exhaust duct가 연소기 길이 방향으로 계속 존재하기 때문에 이에 대한 영향을 최소화시키기 위해 orifice를 장착하였으며 이에 대한 영향 또한 파악하였다. 연소실에 영향을 미칠 수 있는 두 가지 공진주파수를 구하여 이들이 일치하는 지점을 파악하여 공진주파수의 영향이 강하게 나타날 수 있는 가능성이 높은 조건을 파악하였다. 이에 대해 속도 섭동의 크기 변화를 통해 공진주파수의 영역이 가장 큰 지점에 대해 파악하다. 외부 교란이 없을 때 연소실의 압력 섭동이 발생하는 조건을 파악하였으며, 이 조건에서 압력 섭동이 발생하는 원인에 대해 분석하였다. 속도 섭동의 변화를 통해 파악한 연소실에 영향을 미치는 공진주파수들의 교차점과 공기 공급 파트의 공진주파수, 열린 경계에서의 화염전달함수 등을 종합적으로 고려했을 때 압력 섭동이 발생하는 조건과 부합하는 것을 확인하였다.

상기 연구를 통하여 Burke-Schumann flame의 동특성 뿐만 아니라 확산 화염의 연소불안정 발생 메커니즘을 밝히는 연구의 선행연구자료로 활용될 수 있을 것으로 기대된다.

**중심어:** 연소불안정, 비예혼합화염, 확산화염, 제트화염, Burke-Schumann 화염, 화염동특성, 화염전달함수, 화염묘사함수, 비선형적 동특성, 공진주파수, 압력섭동, OH PLIF

학 번: 2011-20701